SYNTHESIS, STRUCTURES, ELECTRONIC STRUCTURES AND PHYSICAL PROPERTIES OF QUATERNARY ALKALI, ALKALINE EARTH, RARE EARTH AND TRANSITION METAL PNICTIDES

by

Yi Wang

A thesis submitted to the Faculty of the University of Delaware in partial fulfillment of the requirements for the degree of Master of Science in Chemistry and Biochemistry

Summer 2015

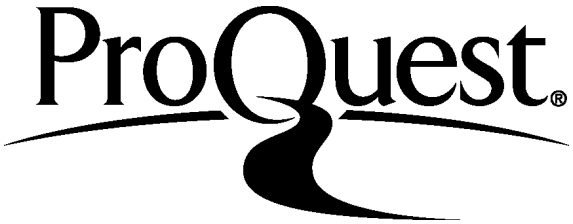

SYNTHESIS, STRUCTURES, ELECTRONIC STRUCTURES AND PHYSICAL PROPERTIES OF QUATERNARY ALKALI, ALKALINE EARTH, RARE EARTH AND TRANSITION METAL PNICTIDES

by

Yi Wang

Approved: _____
Svilen S. Bobev, Ph.D.
Professor in charge of thesis on behalf of the Advisory Committee

Approved: _____
Murray V. Johnston, Ph.D.
Chair of the Department of Chemistry and Biochemistry

Approved: _____
George H. Watson, Ph.D.
Dean of the College of Arts and Sciences

Approved: _____
James G. Richards, Ph.D.
Vice Provost for Graduate and Professional Education

ACKNOWLEDGMENTS

Foremost, I would like to express the deepest appreciation to my advisor Dr. Bobev for giving me the opportunity to study in his laboratory. His infectious passion and professional attitude have been major driving forces through my graduate career in the University of Delaware. I am extremely grateful for his guidance, suggestions and persistent help in these years. Without his important contribution this thesis would not have been possible.

I would like to thank the Department of Chemistry and Biochemistry at University of Delaware for the financial support. And my sincere thanks also go for Dr. Burmeister for his help, understanding and offering my summer teaching opportunity in the Department.

I would like to thank the past and current members of Dr. Bobev's group, Dr. Hua He, Dr. Nian-Tzu Suen, Dr. Marion Schäfer, Dr. Jiliang Zhang, Dr. Stanislav Stoyko, Dr. Julien Makongo, Mr. James Hoos, Mr. Matt Broda and Mr. Greg Darone. They always support and help me in different ways and I really learn lots of experiences and experimental skills from them.

In addition I would like to thank all researchers, technicians, and staffs, who provide all kinds of support and help for me, especially to Dr. Yap, who helps me with single-crystal X-ray diffractometer and Robert Schmidt, who helps me with Physical Property measurement system (PPMS) measurements. And a thank you to all my friends in the department of Chemistry and Biochemistry, I really appreciate their help and cherish our friendships and time we spent together.

Last but not least, I would like to acknowledge with the love and support of my family—my parents Jianping Wang and Yiling Li and my husband Bin Fang. They all keep me going through my life. Without their care and love, I could be who I am right now.

TABLE OF CONTENTS

LIST OF TABLES

LIST OF FIGURES

ABSTRACT

Exploration of new materials and understanding the relationship among compositions, structures and physical properties are still a challenge in solid-state chemistry. Based on the Zintl concepts, studing the crystal structures and electronic structures of Zintl phases, it provides a way to further understand and predict the physical properties of solid state materials. Therefore, we systematically investigated a series of quaternary intermetallic compounds containing alkaline, alkaline-earth, rare earth, transition metals, group 13 and 15 elements. By using powder and single crystal X-ray diffractions, the compositions and crystal structures of these phases could be determined. The electronic structures were also calculated from tight-bonding linear-muffin-tin-orbital (TB-LMTO). The physical properties, which include magnetic susceptibilities and electrical resistivities of the compounds were also reported and discussed.

This work is divided into two chapters: (1) quaternary pnictides with complex, noncentrosymmetric structures: Synthesis and Structural Characterization of the New Zintl Phases

$Na_{11}Ca_2Al_3Sb_8$, $Na_4CaGaSb_3$, and $Na_{15}Ca_3In_5Sb_{12}$. In this chapter, three new Zintl phases were represented: $Na_{11}Ca_2Al_3Sb_8$, $Na_4CaGaSb_3$, and $Na_{15}Ca_3In_5Sb_{12}$. By discovery of different types of Na cations, which include interlayer and intralayer Na atoms, it provides new examples to prove the importance of cations in chemical bonding and structure formation in Zintl phases. (2) Efficient Tailoring of Band Gap Induced by Rare Earth (*RE*) Metals Doping: Determining Structure and Properties of Narrow-Gap Semiconductor $Ca_{9-x}RE_xMn_4Sb_9$ (*RE* = La, Ce, Pr, Nd and Sm). Several numbers of a new structure family, $Ca_{9-x}RE_xMn_4Sb_9$ (*RE* = La, Ce, Pr, Nd and Sm) were synthesized. Due to rare earth

inclusion, electrical resistivity of this series showed semi-conductive behavior with very narrow-band gap, compared with poor metallic material $Ca_9Mn_4Bi_9$.

Chapter 1

INTRODUCTION

1.1 Background

The study of materials has been attractive for scientists from last century due to their amazing properties and potential applications. In general, the study of materials can be divided into two groups: structure and physical properties. Some materials represent interesting properties, such as thermo-electricity [1], superconductivity [2], giant magnetoresistance [3] and quntum confinement [4]. Determination of the relationship between structure and properties is important for chemists, which inspire them to devote tremendous efforts to explore and explain those phenomena. And after years of systematic studies, the derived conclusion is "for a given structure, understanding the connectivity and the arrangement of structural elements creates the ability to explain and even predict certain physical properties" [5]. The famous example is graphite and graphene. Form their names, these two words are similar and related to each other. For the former one, as we know, graphite is conductive. Graphite has a layered 2D structure, which is arranged in a honeycomb lattice. From its crystal structure, atoms in the plane are bonded covalently, and only three of the four potential bonding sites are satisfied. Therefore the fourth electron is free to run in the plane, making graphite electrically conductive. However, compared with graphite, graphene is a zero-gap semi-conductor, which attracted lots of attention in material science during recent years. And due to the contribution of the success in isolating graphene sheets from graphite by tape, Dr. Geim and Dr. Novoselov got the Nobel Prize in Physics for 2010. Graphene is described as single-layer carbon foils. Based on its

unique structure, in which conduction and valence bonds meet at the Dirac points, graphene shows zero-gap semiconductor properties. From the above discussion, it indicates the study of structure provides the way to understand the intrinsic properties of materials.

Generally, there are no rules to directly explain the complicated structures of materials, while simple electron counting rules, such as octet rule and 18-electron rule are very useful to study molecular and solid state compounds. However, when considering metals and intermetallic phases, which would be discussed in the following section, valence rules also need to be considered. Therefore, the study of structure of intermetallic compounds and Zintl phases and the corresponding properties remains a challenge in material field.

1.2 Intermetallic Compounds and Zintl Phases

Intermetallic compounds were defined as solid phases containing two or more metallic elements, with optionally one or more non-metallic elements in 1967 by Dr. Schulze [6]. Unlike alloys, intermetallic compounds usually defined stoichiometry and ordered crystal structure. It can be generally classified into electron (Hume-Rothery phase) phases, size packing phases (such as Laves and Frank-Kasper phase and Nowotny phases), polar intermetallic phases and Zintl phases.

Considering the difference of electronegativtity, we will introduce electron phases and size packing phases firstly based on their small difference of electronegativity among elements.

The first class of intermetallic compounds is the electron phases, which could also be called Hume-Rothery phase. The formation and stability of these compounds could be explained by Hume-Rothery rules, which contains two parts of rules: first one refers to substitutional solid solutions, while the other is about interstitial solid solutions. Generally, the valence electron concentration plays an important role in the phase formation and stability. The typical example is Cu-Zn systems. From the previous study [7], we know the characteristic ratios of valence electrons to atoms for the β-brass, γ-brass and ε-brass are 3/2, 2/3 and 7/4 respectively.

The second important class is Laves and Frank-Kasper phase, which has the general chemical formula AB_2 and could be divided into three types, $MgCu_2$ type (*fcc*), $MgNi_2$ (*hcp*) and $MgZn_2$ (*hcp*) [8]. These intermetallic compounds usually exhibit densest packing and the highest possible coordination and symmetry.

The above two classes show little difference of electronegativity between elements. Considering increase of electronegativity, electropositive and electronegative metals co-exist in the structure, which results in more directional bonds existing in the structure, these class of intermetallic compounds is defined as "polar intermetallics" [9-11]. Thus, obviously in this class, not only normal valence compounds exist. Zintl phases compounds could by also found in this class. Compared with Zintl phases, in general, the difference of electronegativity of polar intermetallics is smaller. However, there is no specific critical value of difference of electronegativity that separates Zintl phases from polar intermetallics.

Last but not least, Zintl phases named by German scientist Eduard Zintl due to his great contribution to this chemical field [12-16]. Generally speaking, Zintl phases

are those compounds composed of electropositive metals (e.g. alkali metals, alkaline earth metals, and rare earth metals) and electronegative metals around the "Zintl line". Inspired by the Grimm Sommerfeld idea to understand III–V semiconductors, "pseudo atom approach" was proposed by Dr. Klemm, which was later refered to Zintl-Klemm concept [17], which indicates valence electron transfer from electropositive to electronegative atoms and covalent interactions involved in compounds. As we know, the first example of Zintl phases was NaTl by Zintl [15]. According to the difference of electronegativity, it is obvious Na could donate one valence electron to Tl and achieve octet configuration Na^+. After gaining one electron for Na, Tl has four electrons in its valence shell, which could further bond to other four around Tl atoms and also achieve octet configuration and form a diamond-like polyanionic framework. Therefore, it is clear that Zintl phases are the link between normal valence compounds and classic salts.

In general, Zintl phases could contain alkali, alkaline-earth metals, rare earth metals, transition metals, and semi-metals from group 13 (Tr, triels), 14 (Tt, tetrels) and 15 (Pn, pnictides) elements. They are charge-balanced compounds: the electropositive atoms are cations and electronegative atoms are anions (or form polyanions), both of which achieve octet configurations. The cations perform like electron donors, charge balancers, and spacers. While the anions frameworks (or polyanions) are held together by "covalent" interactions, their structures can be rationalized with the well-known electron counting rules such as the octet rule.

Due to electron transfer and covalency in compounds consisting of metallic or semimetallic elements, Zintl-Klemm concept is successful on explanation of

relationship between compositions, structures and physical properties for many Zintl and polar intermetallic phases. For example, $Eu_{21}Zn_4As_{18}$ and $Eu_{21}Zn_4Sb_{18}$ [18], they have different structure types. For $Eu_{21}Zn_4As_{18}$, which adopts the β-$Ca_{21}Mn_4Sb_{18}$ structure type, which $Eu_{21}Zn_4Sb_{18}$ crystallizes with the $Ba_{21}Cd_4Sb_{18}$ structure type [19]. The former one can be viewed as 84 Eu^{2+} cations, 16 isolated As^{3-} anions, 6 $[As_2]^{4-}$ dumbbells and two $[Zn_8As_{22}]^{48-}$ subunits per unit cell. While for $Eu_{21}Zn_4Sb_{18}$, compared with $Eu_{21}Zn_4As_{18}$, it contains 168 Eu^{2+} cations, 32 isolated Sb^{3-} anions, 8 $[Sb_2]^{4-}$ dumbbells, and 8 $[Zn_4Sb_{12}]^{26-}$ subunits per unit cell. Both compounds are charge balanced, so we can predict they should be semiconductors, which was proved later by the electric resistivity measurements.

However, limitations of Zintl-Klemm concept results from its oversimplification. Considering the above example, Zintl-Klemm concept fails to explain why $Eu_{21}Zn_4As_{18}$ and $Eu_{21}Zn_4Sb_{18}$ adopt different structure types. For instance, Zintl-Klemm concept has not yet considered ionicity and metallicity. For ionicity, although there is valence electron transfer from electropositive to electronegative atoms, ionic interactions between "cations" and "anionic" frameworks are not considered. There are metallic interactions between positively charged atoms. And their highly delocalized valence electrons, are not considered at all, which further indicates cations not only play a role as electron donors, charge balancers, and spacers, but also have an important effect on structure preference.

1.3 Cation Effect and Exploratory Studies of Quaternary Pnictides with Alkali-Alkaline Earth or Rare-Earth Metals and Transition Metals

To better understand the Zintl phases, specially for cation effect in the structure, our group have systematically investigated many compounds. For example, in our previous study, except "21-4-18" discussed above, we found the pair of isoelectronic compounds Yb_2CdSb_2 and Ca_2CdSb_2, which also adopt different structures: Yb_2CdSb_2 crystallizes in space group *Cmc2₁*, whereas Ca_2CdSb_2 adopts *Pnma* [20].

Recently, we switched to quaternary system. In order to study the role of the cations as structure directing factors, we also synthesized of a new family of Zintl phases Na_2ACdSb_2 and K_2ACdSb_2 (A=Ca, Sr, Ba, Eu, Yb) [21]. With two alkali atoms replacing one alkaline-earth atom, this series are novel isoelectronic and isostructural phases, which crystallize in their own type with space group *Pmc2₁*. This work motivated us to extend our research and seek more new structure for deeper understanding cation effect in Zintl phases [22]. Considering divalent Cd, by replacing with trivalent elements, we may have different structures. Therefore, in this thesis we proceeded experiments: through group 13 elements (Tr, triels) instead of Ca, we found new structures and also discussed the cation effect in structure preference. Their structures boast different structure types and feature: two-dimensional $[InSb_2]$ layers in $Na_{15}Ca_3In_5Sb_{12}$; one-dimensional $[GaSb_3]$ helical chains in $Na_4CaGaSb_3$ and isolated $[Al_3Sb_8]$ trimeric species in $Na_{11}Ca_2Al_3Sb_8$. There are two types of cation Na atoms found in the structure: interlayer and intralayer Na atoms. "Intralayer" Na atoms bulid up $[NaSb_4]$ tetrahedra, which not only act as electron electron donors or spacers, but

also directly impact the structure adoption. More discussion and details could be found in Chapter 1.

In this thesis, we also studied the effects of doping on the physical properties of our materials. On one hand, as we discussed above, due to its specific station, Zintl phases are neither covalent nor ionic compounds, which usually exhibite as poor metallic or semi-conductive properties. On the other hand, it is well known that doping is an efficient way to alter the conductivity of semiconductors by introducing impurities: greatly increasing additional charge carriers into materials [23-27]. $Ca_9Mn_4Bi_9$ [28] structure was considered to be appropriate in our exploration. According to Zintl concept, this structure could be described as 9 Ca^{2+} cations and 1 $[Cd_4Sb_9]^{19-}$ subunit, which totally had one extra negative charge from $[Cd_4Sb_9]^{19-}$, which performed like poor metal. In order to achieve charge-balanced, $Ca_9Zn_{4+x}Sb_9$ [29] was successfully synthesized, which had additional one electron from extra Zn. Inspired by our previous work, rare earth (*RE*) metals doping is considered here to be another possible way because of *RE* metals, except Eu and Yb (divalent), usually represented trivalent in intermetallic compounds. Finally, $Ca_{9-x}RE_xMn_4Sb_9$ (*RE* = La, Ce, Pr, Nd and Sm) series compounds were constructed and successfully synthesized, which were crystalized in a new structure type with the orthorhombic space *Pbam*. Compared with parent structure $Ca_9Mn_4Bi_9$, containing 2 Mn sites, the most remarkable point was that in the *RE* doped structure: there are three Mn sties. According to the Zintl-Klemm concept, this series are supposed to be semiconductive compounds, a notion that was supported by reliable resistivity data. More details and information could be found in Chapter 2.

1.4 Layout of The Thesis

This thesis reports 8 new compounds, which contains alkaline, alkaline-earth, rare-earth metals, transition metals, group 13 and 15 elements. Their crystal structures were determined from powder and single crystal X-ray diffraction data were acquired on a Bruker SMART and APEX 2 CCD-based diffractometer (monochromatized Mo $K\alpha$ radiation, λ=0.71073 Å). The programs SMART and SAINT [30] was used to process data. Program SADABS was also used for the semi-empirical absorption correction [31]. The structures were refined with the full-matrix least squares on the F^2 method, as implemented in SHELXTL [32]. Before the final refinement steps, the atomic positions were standardized by STRUCTURE TIDY [33]. The electronic structures were carried out from tight-bonding linear-muffin-tin-orbital (TB-LMTO) [34, 35]. Field-cooled (FC) direct-current (DC) magnetization measurements were performed in a Quantum Design PPMS. By using four probes method, the measurements of electrical resistivity were also done with the PPMS. This dissertation contains two chapters mentioned above, which follow the introduction section:

Chapter 1: Quaternary Pnictides with Complex, Noncentrosymmetric Structures. Synthesis and Structural Characterization of the New Zintl Phases $Na_{11}Ca_2Al_3Sb_8$, $Na_4CaGaSb_3$, and $Na_{15}Ca_3In_5Sb_{12}$. *Inorg. Chem*. **2015**, *54*, 1931.

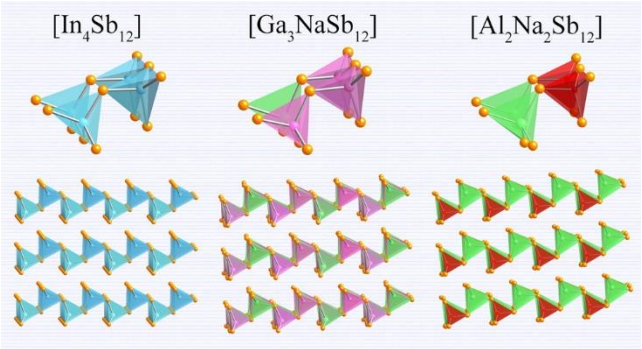

Chapter 2: Efficient Tailoring of Band Gap Induced by Rare Earth (*RE*) Metals Doping–Determining Structure and Properties of Narrow-Gap Semiconductor $Ca_{9-x}RE_xMn_4Sb_9$ (*RE* = La, Ce, Pr, Nd and Sm)

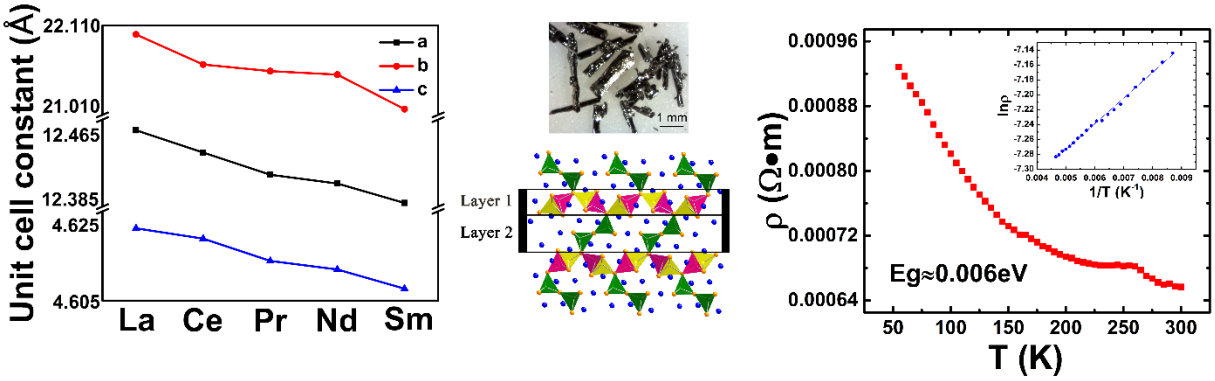

Finally, a brief conclusion of these systems will be performed in the end.

REFERENCES

1. Satterthwaite, C. B.; Ure, R. *Phys. Rev*. **1957**, *108*, 1164.

2. Bardeen, J.; Cooper, L. N.; Schrieffer, J. R. *Phys. Rev*. **1957**, *108*, 1175.

3. Pecharsky, V. K.; Gshneidner, K. A. Jr. *Phys. Rev. Lett*. **1997**, *78*, 449.

4. Wang, C.; Shim, M.; Guyot-Sionnest, P. *Science*, **2001**, *291*, 2390.

5. Miller, G. J. Structure and Bonding of Zintl Phases and Inos; Kauzlarich, S., Ed.; VCH Publishers, Inc.: New York, **1996**, P. 1.

6. G. E. R. Schulze: Metallphysik, Akademie-Verlag, Berlin **1967**.

7. Hume-Rothery, W. J. *Inst. Metals.* **1926**, *35*, 309.

8. Villars, P.; Calvert L. D. (Ed.), Pearson's Handbook of Crystallographic Datafor Intermetallic Phases, ASM International, Materials Park, OH, 2nd edn., **1991**.

9. Schäfer, H. *Ann. Rev. Mat. Sci*. **1985**, *15*, 1 and references within.

10. Corbett, J. D. *Chem. Rev*. **1985**, *85*, 383 and references within.

11. Corbett, J. D. Structure and Bonding **1997**, *87*, 157.

12. Zintl, E. Naturwiss. **1929**, 17, 781.

13. Zintl, E.; Dullenkopf, W. Z. *Phys. Chem*. **1932**, *B16*, 183.

14. Zintl. E.; Brouer, G. Z. *Phys. Chem*. **1933**, *B20*, 245.

15. Zintl, E.; Woltersdorf, G. Z. *Electrochem*. **1935**, *41*, 876.

16. Zintl, E. *Angew. Chem*. **1939**, *52*, 1.

17. Klemm, W.; Busmann, E. Z. *Anorg. Allg. Chem*. **1963**, *319*, 297

18. Suen, N. T.; Wang, Y.; Bobev, S. *J. Solid State Chem*. **2015**, *227*, 204.

19. Xia, S. Q.; Bobev, S. *Inorg. Chem*. **2008**, *47*, 1919.

20. Xia, S. Q.; Bobev, S. *J. Am. Chem. Soc*. **2007**, *129*, 4049.

21. Saparov, B.; Saito, M.; Bobev, S. *J. Solid State Chem*. **2011**, *184*, 432.

22. Wang, Y.; Stoyko, S.; Bobev, S. *Inorg. Chem*. **2015**, *54*, 1931.

23. Cahen, D. *Chem. Mater*. **1998**, *10*, 2596.

24. Suh, J.; Park, T. E.; Lin, D. Y.; Fu, D. Y.; Wu, J. Q. *Nano Lett*. **2014**, *14*, 6976.

25. Valentin, C. D.; Pacchioni, G.; Selloni, A. *Chem. Mater*. **2005**, *17*, 6656.

26. Jorge, M. E. M.; Nunes, M. R.; Maria, R. S.; Sousa, D. *Chem. Mater*. **2005**, *17*, 2069.

27. Carvalho, M. D.; Borges, R. P.; Godinho, M. *Chem. Mater*. **2005**, *17*, 4852.

28. Brechtel, E.; Cordier, G.; Schäfer, H. Z. *Naturforsch. B.* **1979**, *34*, 1229.

29. Xia, S. Q.; Bobev, S. *J. Am. Chem. Soc*. **2007**, *129*, 10011.

30. SMART and SAINT; Bruker AXS Inc.: Madison, WI, **2002**.

31. Sheldrick, G. M. SADABS. University of Göttingen, Germany, **2003**.

32. Sheldrick, G. M. SHELXTL. University of Göttingen, Germany, **2001**.

33. Gelato, L. M.; Parthe, E. STRUCTURE TIDY– a computer program to standardize crystal structure data. *J. Appl. Crystallogr*. **1987**, *20*, 139.

34. (a) Andersen, O. K. *Phys. Rev. B.* **1975**, *12*, 3060. (b) Andersen, O. K.; Jepsen, O. *Phys. Rev. Lett*. **1984**, *53*, 2571. (c) Andersen, O. K. *Phys. ReV. B.* **1986**, *34*, 2439. (d) Skriver, H. L. The LMTO Method; Springer, Berlin, **1984**.

35. Jepsen, O.; Andersen, O. K. The Stuttgart TB-LMTO Program, Version 4.7.

Chapter 2

QUATERNARY PNICTIDES WITH COMPLEX, NONCENTROSYMMETRIC STRUCTURES. SYNTHESIS AND STRUCTURAL CHARACTERIZATIN OF THE NEW ZINTL PHASES $Na_{11}Ca_2Al_3Sb_8$, $Na_4CaGaSb_3$, and $Na_{15}Ca_3In_5Sb_{12}$

2.1 Abstract

Three new Zintl phases, $Na_{11}Ca_2Al_3Sb_8$, $Na_4CaGaSb_3$, and $Na_{15}Ca_3In_5Sb_{12}$, have been synthesized by solid-state reactions, and their structures have been determined by single-crystal X-ray diffraction. $Na_{11}Ca_2Al_3Sb_8$ crystallizes with its own structure type (Pearson index *oP48*) with the primitive orthorhombic space group $Pmn2_1$ (No. 31). The structure is best viewed as $[Al_3Sb_8]^{15-}$ units of fused $AlSb_4$ tetrahedra, a novel type of Zintl ion, with Na^+ and Ca^{2+} cations that solvate them. $Na_4CaGaSb_3$ also crystallizes in its own type with the primitive monoclinic space group *Pc* (No. 7; Pearson index *mP36*), and its structure boasts one-dimensional $[GaSb3]^{6-}$ helical chains of corner-shared GaSb4 tetrahedra. The third new compound, $Na_{15}Ca_3In_5Sb_{12}$, crystallizes with the recently reported $K_2BaCdSb_2$ structure type (space group $Pmc2_1$; Pearson index *oP12*). The $Na_{15}Ca_3In_5Sb_{12}$ structure is based on polyanionic layers made of corner-shared InSb4 tetrahedra. Approximately one-sixth of the In sites are vacant in a statistical manner. All three structures exhibit similarities to the TiNiSi structure type, and the corresponding relationships are discussed. Electronic band structure calculations performed using the tight-binding linear muffin-tin orbital atomic sphere approximation method show small band gaps for all three compounds, which suggests intrinsic semiconducting behavior for these materials.

2.2 Introduction

The compounds formed between the alkali or alkaline-earth metals and the post-transition elements from groups 13−15 are typically referred to as Zintl phases [1, 2]. Using the Zintl−Klemm

concept, the structures of such materials are readily rationalized as cations (less electronegative elements) and anions (more electronegative elements), so that the valence rules are satisfied Recently, our group has investigated quite a few new cases of presumed Zintl phases, where the cations can be seen as intimately involved in the chemical bonding; for example, $A_{21}Cd_4Sb_{18}$ (A = Eu, Ba) [3] and A_2CdSb_2 (A = Ca, Yb) [4] are two kinds of structures in which the cations proved to be important structure-directing parameters (for the same valence electron count). The series Ba_2ZnPn_2 (Pn = As, Sb, Bi) [5] not surprisingly, demonstrated that for the same structure and valence electron count mixing of the cation and anion states is responsible for the transition from intrinsic semiconducting behavior to metallic behavior as the sizes and electronegativities of the atomic partners are varied. The cited examples are yet another testament to the notion that "closed-shell species", "electron donors/acceptors", "space fillers", etc., which are traditional terminology in the Zintl−Klemm concept, are somewhat far from reality.

The previous work motivated us to extend our research and to seek more new structures with complex bonding characteristics. The fact that in recent years many ternary antimonides have gained interest as prospective materials for applications in thermoelectric energy conversion [6−8] is another reason why we were attracted to the ongoing research efforts in this general area. Herein, we report the results from a new direction of this project, which includes the identification and the characterization of three new Zintl phases:

$Na_{11}Ca_2Al_3Sb_8$, $Na_4CaGaSb_3$, and $Na_{15}Ca_3In_5Sb_{12}$. They provide new examples for the significant role of cations in chemical bonding and structure formation in Zintl phases. The focus of this paper is on the synthesis, the single-crystal X-ray diffraction studies, and the electronic structures (calculated by the tight-binding linear muffin-tin orbital atomic sphere approximation (TB-LMTOASA) method [9]) of the three new compounds. The structural similarities among them are presented; the close structural relationship to the TiNiSi structure type (also known as the Co_2Si type [10]) is discussed as well.

2.3 Experimental

Synthesis. Because of the high sensitivity of elemental Na to air and moisture, handling of the starting materials required extreme caution. All manipulations were carried out inside an Ar-filled glovebox with a controlled atmosphere or under vacuum. The metals were purchased from Alfa or Aldrich (purity >99.9%) and were used as received. The Na surface was scrapped off with a scalpel blade immediately before use.

Single crystals of the title compounds were first identified from exploratory reactions of the corresponding elements Na, Ca, Tr, and Sb in the molar ratio of 3:3:1:4 (Tr = Triel, i.e., a group 13 element). The metals were weighed in the glovebox (total weight ca. 500 mg) and loaded into Nb tubes, which were then closed by arc welding under high-purity Ar gas. The sealed Nb containers were subsequently jacketed within evacuated fused-silica tubes. The reaction mixtures were heated to 1173 K at a rate of 100 K/h and equilibrated at this temperature for 24 h. Following a cooling step to 773 K at a rate of 5 K/h, the products were brought to room temperature over 12 h. On the basis of analysis of the single-crystal and powder X-ray diffraction data, multiple binary, ternary, and quaternary phases were obtained in each case. Besides $Na_{11}Ca_2Al_3Sb_8$, $Na_4CaGaSb_3$, and

$Na_{15}Ca_3In_5Sb_{12}$, we were also able to identify $Na_3Ca_3AlSb_4$ [11], $Ca_5Ga_2Sb_6$ [12], Na_3InSb_2 [13], $Ca_{11}Sb_{10}$ [14], and NaSb [15] among some other, yet unidentified phases.

After the structures and chemical compositions were established by single-crystal work, new reactions with the proper stoichiometry were loaded. They yielded the desired compounds as major products. The produced samples contained small amounts of impurity phase(s), but the bulk consisted of small, shiny crystals with a dark-metallic luster that were the targeted phases. The materials were brittle and air sensitive.

We speculated that the three newly identified phases might have isostructural "neighbors" within the arsenides or bismuthides. Such reactions were set up, and the corresponding products were analyzed–no isostructural arsenides or bismuthides were found; instead, we uncovered new phases with different structures, which will be the subject of a forthcoming publication. We also explored periodic trends by changing the alkali and/or alkaline-earth metal and will detail the results from this work in another follow-up article.

Caution! At the aforementioned conditions, Na metal will evaporate and could create high pressure. It is therefore important to use as long as possible Nb containers (3/8 in. in diameter and ca. 5/2 to 3 in. in length) and long f used-silica tubes (7/8 in. in diameter and ca. 10−12 in. in length), which must be left protruding outside the furnace. Doing so minimizes the risk of serious accidents because, in the case of a leak, the Na vapors will diffuse and condense at the cold end of the f used-silica tube. If this happens, the furnace must be stopped immediately.

Powder X-ray Diffraction. The as-synthesized samples were ground in the glovebox to fine powders. Then, powder X-ray diffraction patterns were taken at room

temperature on a Rigaku MiniFlex powder diffractometer using filtered Cu *Kα* radiation (λ = 1.54056 Å), also operated inside the glovebox. Data analysis was done using the JADE 6.5 software package.

Because of the limited capabilities of the MiniFlex, combined with the low symmetry and complex nature of the structures, the patterns had many peaks that could not be well-resolved. Therefore, the powder X-ray diffraction patterns were only used for phase identification; all reported cell parameters were refined by single crystal X-ray diffraction data.

Single-Crystal X-ray Diffraction. The single-crystal X-ray diffraction experiments were done on a Bruker SMART CCD-based diffractometer with a three-circle goniometer, employing monochromatized Mo *Kα* radiation (λ = 0.71073 Å). During the data collection, the temperature was kept at 200 K by a cold N_2 stream. Maintaining an inert atmosphere during the experiments was critical because the crystals deteriorate very quickly if exposed to the laboratory air (all preparations were done in a glovebox with an optical microscope and under dried Paratone N oil). Data acquisition and integration were completed using the programs *SMART* and *SAINT*, supplied by Bruker [16]. Semiempirical absorption correction based on equivalent reflections was applied using *SADABS* [17]. The structures were solved by direct methods and refined with a full-matrix least-squares method on F^2, as implemented in *SHELXTL* [18]. The refinements converged readily to low conventional residuals and final difference Fourier maps, which were flat. Refined parameters included the scale factors and atomic positions with the corresponding anisotropic displacement parameters. Where applicable, site occupation factors were also

refined. Additional details pertaining to the structure refinements and the way the mixed occupied sites were handled.

Selected crystallographic information and refinement parameters for $Na_{11}Ca_2Al_3Sb_8$, $Na_4CaGaSb_3$, and $Na_{15}Ca_3In_5Sb_{12}$ are summarized in Table 1.1. Final positional and equivalent isotropic displacement parameters are given in Tables 1.2−1.4. Relevant interatomic distances and angles are listed in Table 1.5. Additional details of the crystal structure investigations may be obtained from the Fachinformationszentrum Karlsruhe, 76344 Eggenstein-Leopoldshafen, Germany [fax (49) 7247-808-666; e-mail crysdata@fiz.karlsruhe.de] with depository numbers CSD 428753 for $Na_{11}Ca_2Al_3Sb_8$, CSD 428754 for $Na_4CaGaSb_3$, and CSD 428752 for $Na_{15}Ca_3In_5Sb_{12}$.

Energy-Dispersive X-ray Spectroscopy (EDX). To verify the refined compositions, selected single crystals from each sample were subjected to EDX analysis. A JEOL 7400 F electron microscope, equipped with an Oxford INCA spectrometer, was employed. The analyses were severely hindered by the air sensitivity of the studied samples, and the obtained data could only confirm the elemental makeup; no quantitative interpretation of the results was possible.

Electronic Structure Calculations. The electronic structure calculations were carried out with the TB-LMTO method9 using the LMTO47 program [19−21]. The total and partial density of states (DOS) and crystal orbital Hamilton population (COHP) [22] curves of selected interactions are presented and discussed. Exchange and correlation terms were treated by the local density approximation [23]. All relativistic effects except spin−orbit coupling were taken into account by using a scalar relativistic approximation. The basis sets including 3s, 3p, and 3d orbitals for Na and Al, 4s, 4p, and 3d orbitals for

Ca and Ga, and 5s, 5p, 5d, and 4f orbitals for In and Sb were treated by the Löwdin downfolding technique [24]. The k-space integrations were conducted using the tetrahedron method [25] and the Fermi level was set at 0 eV as the energy reference.

2.4 Results and Discussion

Structure and Chemical Bonding of $Na_{15}Ca_3In_5Sb_{12}$. We begin our discussion on the chemical bonding by describing the structure of $Na_{15}Ca_3In_5Sb_{12}$, which is the simplest among the three (Figure 1.1a). $Na_{15}Ca_3In_5Sb_{12}$ appears to be the first structurally characterized compound in the quaternary Na−Ca−In−Sb phase diagram; it crystallizes in the orthorhombic space group *Pmc2₁* (Pearson index *oP12*).

$Na_{15}Ca_3In_5Sb_{12}$ (i.e., $Na_2(Na_{0.5}Ca_{0.5})In_{0.83}Sb_2$) is best described as a substitution derivative of the recently reported Zintl phase $K_2BaCdSb_2$ [26] whereby the trivalent In (partially occupied) takes the role of the divalent Cd [27]. Because the important features of this structure have already been discussed [26], in the following paragraphs we will focus on a few details and on the structural relationship to the other two compounds.

There are six crystallographically unique atoms in the asymmetric unit (Table 1.2), which include two Na sites, one mixed-occupied Ca/Na site, one In site, and two Sb sites. The In site, as mentioned already, is not fully occupied, with one-sixth of the positions being randomly vacant. When the disorder is ignored, the structure can be described as infinite $[InSb_2]^{2-}$ polyanionic layers made of corner-shared $InSb_4$ tetrahedra. Defects in the polyanions of the Zintl phases are rare but not without precedent, as demonstrated on the example of $Eu_5Cd_3Sb_6$ [28]. In the latter structure (own type), one-fourth of the Cd positions are randomly vacant.

There are no direct homoatomic interactions. The In−Sb distances range from 2.924(7) to 2.960(8) Å (Table 1.5). Within the tetrahedra, the Sb−In−Sb angles range from 100.18(3)° to 112.41(2)°, attesting to a slight distortion from the ideal tetrahedral geometry. The numerical values for the In−Sb bonds and Sb−In−Sb angles compare well with those reported for other ternary A−In−Sb phases (A = alkali or alkaline-earth metal), such as $Ca_5In_2Sb_6$ [29] and Na_3InSb_2[13]. The In−Sb interatomic distances (Table 1.5) are only ca. 4−6% longer than the sum of their single-bonded Pauling radii (e.g., $r_{In} + r_{Sb} = 1.421 + 1.391 = 2.812$ Å) [30], suggesting appreciable covalent bonding between them.

The structure also contains Na^+ and Ca^{2+} cations, which fill the space between the polyanionic layers. As discussed in a previous paper [26], following the Zintl−Klemm concept [1, 2], the parent $K_2BaCdSb_2$ structure can be rationalized as $(K^+)_2(Ba^{2+})(Cd^{2+})(Sb^{3-})_2$. In the same manner, taking into account the disorder, $Na_{15}Ca_3In_5Sb_{12}$ can also be viewed as a Zintl phase, the formula of which can be expressed as $(Na^+)_{15}(Ca^{2+})_3(In^{3+})_5(Sb^{3-})_{12}$. This argument is nicely supported by the electronic structure calculations, which show opening of a band gap right at the energy where the bonding interactions are optimized (vide infra).

Structure and Chemical Bonding of $Na_4CaGaSb_3$. Upon replacement of the heavier In with the lighter and smaller Ga, the same reaction scheme that produced $Na_{15}Ca_3In_5Sb_{12}$ allowed for the quantitative synthesis of the new phase $Na_4CaGaSb_3$ (=$Na_{16}Ca_4Ga_4Sb_{12}$). As can be inferred from the close compositions, the two structures are similar, although there are distinct differences. The structure is projected in Figure 1.1b; some important similarities and differences between $Na_{15}Ca_3In_5Sb_{12}$ and $Na_4CaGaSb_3$ are shown in Figures 1.2.

$Na_4CaGaSb_3$ crystallizes in its own structure type with the primitive monoclinic space group *Pc* (Pearson symbol *mP36*). The structure contains eight Na, two Ca, two Ga, and six Sb atoms in the asymmetric unit. In analogy to what we already discussed for $Na_{15}Ca_3In_5Sb_{12}$, the two Ca sites here are also mixed-occupied (Table 1.3). The $Na_4CaGaSb_3$ structure can be viewed as one-dimensional $[GaSb_3]^{6-}$ helical chains made up of corner-shared $GaSb_4$ tetrahedra (Figure 1.2b). The chains propagate along the crystallographic c direction, with Na and Ca cations filling the space between them. Importantly, if one considers some of the Na cations, Na3 in the current nomenclature, as part of the polyanionic structure (vide infra), hypothetical $[Ga_{2/3}Na_{1/3}Sb_2]$ layers of corner-shared $GaSb_4$ and $NaSb_4$ tetrahedra can be derived. Such hybrid layers would have the same topology as the previously described $[InSb_2]$ layers made solely of corner shared $InSb_4$ tetrahedra.

The corresponding Ga−Sb distances range from 2.679(3) to 2.891(5) Å (Table 1.5). The range is somewhat wider than expected, and the sum of the Pauling single-bonded radii (e.g., $r_{Ga} + r_{Sb} = 1.246 + 1.391 = 2.637$ Å) [30] confirms that there will be significant variations in the Ga−Sb bonding [31]. The Sb−Ga−Sb angles, which range from 101.58(4)° to 114.02(7)°, also indicate that the $GaSb_4$ tetrahedra are somewhat more distorted than the aforementioned $InSb_4$ tetrahedra, which could be a subtle feature of the Ga−Sb bonding. It appears the former speculation is more likely because this observation is not unprecedented; other ternary A−Ga−Sb phases, such as $Ca_5Ga_2Sb_6$ [12] and $Na_2Ga_3Sb_3$ [32], whose structures are also based on $GaSb_4$ tetrahedra, show a comparatively wide range of Ga−Sb distances. Just like $Ca_5Ga_2Sb_6$ [12] and $Na_2Ga_3Sb_3$ [32] the new compound $Na_4CaGaSb_3$ is also a Zintl phase, which can be rationalized as $(Na^+)_4Ca^{2+}Ga^{3+}(Sb^{3-})_3$.

Structure and Chemical Bonding of $Na_{11}Ca_2Al_3Sb_8$. The last, and the most dimensionally reduced, structure of all three is that of $Na_{11}Ca_2Al_3Sb_8$. This new compound crystallizes with the noncentrosymmetric orthorhombic space group *Pmn2₁* (Figures 1.1c). Inspection of Pearson's Handbook [10] and the Inorganic Crystals Structure Database (ICSD) [33] reveals that there is no precedent of a structure with the same sequence of Wyckoff letters, suggesting that the $Na_{11}Ca_2Al_3Sb_8$ structure represents yet another novel structure type (Pearson symbol *oP48*). The structure contains six Na, two Ca, two Al, and five Sb atoms in the asymmetric unit. One of the two Ca sites here is mixed-occupied also (Table 1.2).

As emphasized in Figure 1.2c, the most prominent feature of this structure is the $[Al_3Sb_8]^{15-}$ subunit. This molecular-like fragment is first-of-a-kind in the chemistry of the Zintl phases and ions [1, 2] and is built of three $AlSb_4$ tetrahedra, which share edges with each other in a cis-arrangement. The trimers are composed of two tetrahedra that are crystallographically unique; the third one is a symmetry-equivalent image, generated by the mirror plane perpendicular to the *a* direction and passing through the Al atom #2. All Al−Sb distances fall in the range of 2.650(2)−2.777(2) Å (Table 1.5). The range is much narrower than the interval observed for the Ga−Sb distances in $Na_4CaGaSb_3$ (vide supra), and the numerical values match well with the sum of the corresponding Pauling radii (e.g., $r_{Al} + r_{Sb}$ = 1.248 + 1.391 = 2.639 Å)[30]. The Sb−Al−Sb angles vary from 101.32(7)° to 118.22(7)°. All structural metrics compare well with those reported for other structures based on $AlSb_4$ tetrahedra, for instance, $Ca_5Al_2Sb_6$ [34] and $Na_7Al_2Sb_5$ [35] Given the absence of homoatomic interactions, $Na_{11}Ca_2Al_3Sb_8$ can also be classified as a Zintl phase based on the formulation $(Na^+)_{11}(Ca^{2+})_2(Al^{3+})_3(Sb^{3-})_8$.

Structural Relationships. Having discussed the important features of the three structures, we now turn our attention to the structural relationships among them. Briefly, let us recall that $Na_{15}Ca_3In_5Sb_{12}$ boasts two-dimensional $[InSb_2]^{2-}$ polyanionic layers of corner-shared $InSb_4$ tetrahedra (again, not considering the vacant In sites that could account for ribbons if long-range ordered), $Na_4CaGaSb_3$ features one-dimensional $[GaSb_3]^{6-}$ helical chains of $GaSb_4$ tetrahedra, and $Na_{11}Ca_2Al_3Sb_8$ has trimeric $[Al_3Sb_8]^{15-}$ zero-dimensional fragments of fused $AlSb_4$ tetrahedra.

At first glance, there is no connection between the three structures. However, after careful consideration, striking similarities among the three compounds become apparent upon studying the cations' coordination. For example, one can see that in the three structures there are two types of Na atoms: interlayer and intralayer Na atoms, i.e., the atoms residing between and within the layers, respectively. The nuances of the interlayer and intralayer bonding, and the subtly different roles the two types of cations play, have already been discussed on the examples of $Ba_3Cd_2Sb_4$ and its Sr-substituted variant $Ba_{3-x}Sr_xCd_2Sb_4$ [36]. This discussion was subsequently extended along the lines of the coloring of the cation sites by cations with different charges, as in $K_2BaCdSb_2$ [26], which is the prototype of the herein-presented $Na_{15}Ca_3In_5Sb_{12}$. In the $Na_4CaGaSb_3$ and $Na_{11}Ca_2Al_3Sb_8$ structures, which are not layered per se, the "intralayer" Na atoms will be those located beside the $[GaSb_3]^{6-}$ helical chains or the $[Al_3Sb_8]^{15-}$ trimers. In Figure 1.3a, the Na2 atom is shown as surrounded by four Sb atoms in distorted tetrahedral geometry and is positioned between two adjacent helical chains, connecting them by Na−Sb bonds. In Figure 1.3b, Na5 in the $Na_{11}Ca_2Al_3Sb_8$ structure is shown in its tetrahedral coordination

of four Sb atoms. Two such tetrahedra form a dimer, which is connected to surrounding Al_3Sb_8 trimers.

Clearly, the common denominator here is the ability of these Na atoms to participate in covalent-like bonding with the polyanions. In both structures, the intralayer Na is tetrahedrally coordinated with the Na−Sb bonds showing "normal" distances. The Na−Sb distances range from 3.086(2) to 3.207(2) Å in $Na_4CaGaSb_3$ and from 3.078(3) to 3.202(3) Å in $Na_{11}Ca_2Al_3Sb_8$, respectively. The range is similar to the reported distances in $Na_2YbCdSb_2$ (ordered quaternary variant of the Yb_2CdSb_2 structure), where the tetrahedral Na is located ca. 3.1 Å away from its closest neighbors [26]. In another structure type, adopted by at least five more Zintl phases $KA_2Cd_2Sb_3$ (A= Ca, Sr, Ba, Eu, Yb) [37], all K cations are in tetrahedral coordination also, which is not common for such a large ion; they are also tightly coordinated with K−Sb distances as short as 3.36 Å [37]. All of the above-mentioned interatomic distance match well with the sum of the corresponding Pauling single bonded radii (e.g., $r_{Na} + r_{Sb} = 1.572 + 1.391 = 2.963$ Å; $r_K + r_{Sb} = 2.025 + 1.391 = 3.416$ Å).

Including the intralayer Na atoms in the consideration of the polyanions in $Na_4CaGaSb_3$ and $Na_{11}Ca_2Al_3Sb_8$, one can notice that they can be viewed as "hybrid-layered" structures (Figure 1.4). For the $Na_4CaGaSb_3$ structure, the ratio of Ga/Na is 2:1 within the "hybrid layers", while in $Na_{11}Ca_2Al_3Sb_8$, the ratio of Al/Na is 1:1. In the $Na_{15}Ca_3In_5Sb_{12}$ structure, the $[InSb_2]$ layers are "free-standing"; i.e., the Na atoms here are positioned between adjacent layers.

The participation of different amounts of Na atoms in the formation of "hybrid polyanionic layers" could also explain the variations of the Ga−Sb and Al−Sb bond lengths.

As we discussed before, the shortest Ga−Sb bond measures 2.679(3) Å (between Ga2 and Sb5). The second shortest is 2.681(6) Å between Ga1 and Sb1 (Table 1.5). Considering the proximity of the intralayer Na2 atom, which impacts both Ga1 and Ga2 through Sb1 and Sb5, respectively, we can argue that the corresponding Ga−Sb distances ought to be on the short side in order for the structure to "make room" for the more spatially demanding Na. In the $Na_{11}Ca_2Al_3Sb_8$ structure, the shortest Al−Sb bond is 2.650(2) Å and also occurs in the $[Al_2Na_2Sb_{12}]$ subunit (Figure 1.3) between Al1 and Sb2 (Table 1.5). Here, Na5 is affecting Al1 through the Sb2 vertex (Figure 1.3). In analogy with the $[Ga_3NaSb_{12}]$ fragment, it is again reasonable to expect that Al1−Sb1 will be "squeezed" and would be the shortest bond with the $AlSb_4$ tetrahedra.

Relationship to the Common TiNiSi Structure Type. A different description of these structures can be proposed on the basis of their close relationship with the ubiquitous TiNiSi structure type (also referred to as the Co_2Si structure type) [10]. The compound $Na_3In_2Bi_3$ [$NaIn_{0.67}Bi$ = (Na^+) $(In^{3+})_{0.67}(Bi^{3-})$ [38] is known to form with this structure (Figure 1.5a), and it can be described as a polyanionic InBi framework (note that, for simplicity, the defects on the In sites are not considered here) with Na^+ cations filling the channels within it. Figure 1.5b depicts the structure of $Na_{15}Ca_3In_5Sb_{12}$, where the Na−Sb bonds (tetrahedral ones) are shown to guide the eye, as well as the bonds between In and Sb (differentiated in light blue). By comparing the two images, one can see that $Na_{15}Ca_3In_5Sb_{12}$, reformulated as $Na_9Ca_3(In_5Na_6)Sb_{12}$, or notwithstanding the defects on the In site as $(Na_{0.75}Ca_{0.25})(In_{0.5}Na_{0.5})Sb$, is a variant of the same structure; the "coloring" of the atomic positions describing the framework is different. Figure 1.5c shows $Na_4CaGaSb_3$ drawn in a similar manner (can be reformulated as $Na_2Ca(GaNa_2)Sb_3$, or rather

($Na_{0.67}Ca_{0.33}$)($Ga_{0.33}Na_{0.67}$)Sb). Figure 1.5d is a representation of the $Na_{11}Ca_2Al_3Sb_8$ structure, where the relationship to the "parent" is the most complicated among all three, yet composing similar Al−Na−Sb hybrid layers allows for the structure to be viewed as $Na_6Ca_2(Al_3Na_5)Sb_8$, or ($Na_{0.75}Ca_{0.25}$)($Al_{0.375}Na_{0.625}$)Sb if normalized to the 1:1:1 stoichiometry. Note also that, for ease of viewing, the ordering of the Na and Ca atoms filling the channels (in all cases) has been exaggerated.

Electronic Structure. The calculated DOS are presented in Figure 1.6; the COHPs for selected atom pairs are projected in Figure 1.7. For all three structures, idealized models were considered, whereby the mixed-occupied Na/Ca positions were treated as either Na or Ca, and then the Fermi level was adjusted to the correct number of valence electrons per formula unit. For $Na_{15}Ca_3In_5Sb_{12}$, where in addition to the Na/Ca disorder partial occupancy on the In site is also observed (vide supra), we used the idealized, stoichiometric formula $Na_2CaInSb_2$ (as in the archetype $K_2BaCdSb_2$ [26]) and then integrated the DOS for the experimental number of valence electrons and placed the Fermi level accordingly.

As shown in Figure 1.6, the DOS plot of $Na_{15}Ca_3In_5Sb_{12}$ is much simpler than those of $Na_4CaGaSb_3$ and $Na_{11}Ca_2Al_3Sb_8$, which is apparently due to the greater complexity of the latter two structures. As discussed before, there are only six unique atoms in the asymmetric unit of the $Na_{15}Ca_3In_5Sb_{12}$ structure, while $Na_4CaGaSb_3$ and $Na_{11}Ca_2Al_3Sb_8$ have nearly three times as many. Notwithstanding the differences in the general appearance of the curves, one can notice that there is a small energy gap between the top of the valence band and the bottom of the conduction band, which indicates small-gap semiconductor properties. Compared with that, the band gap in $Na_4CaGaSb_3$ is larger, as expected for a compound with the less electronegative Ga (χGa = 1.6; χIn = 1.7 on the

Pauling scale [30]). Similarly, the band gap widens a bit more for $Na_{11}Ca_2Al_3Sb_8$ (χAl = 1.5 on the Pauling scale [30]). Such a comparison of the calculated band gaps, of course, should be taken with caution because the three compounds under consideration are not isotypic and there are marked differences in their structures. We also need to acknowledge the relatively small amount of the Tr element in the structures and the fact that Sb and Na/Ca electronic states dominate on both sides of the band gap; in that sense, the notion that the choice of the Tr element will strongly influence the size of the band gap can be easily refuted. The calculated band gaps vary from 0.05 to 0.75 eV, which could mean that some of these compounds (or their properly designed solid solutions) could be potentially good thermoelectric materials, a speculation that comes about from recognizing that similar antimonide compounds are well known as high-efficiency thermoelectric materials [6−8].

The states just below the Fermi levels in $Na_{15}Ca_3In_5Sb_{12}$ are predominately from the contribution of the Sb 5p orbital. Judging from the COHPs, the contribution from the Ca and Na states is limited, which means their roles are largely of electron donors, as in the classical Zintl description. This is not quite true for $Na_4CaGaSb_3$ and $Na_{11}Ca_2Al_3Sb_8$, where the Sb 5p states still have the major contribution; however, the relative contributions from Na and Ca to the total DOS appear to increase. Given that there are Na/Ca atoms in tetrahedral voids (recall the interlayer Na vs intralayer Na atoms; Figure 1.3), the implied higher degree of covalence is not difficult to understand. We can relate this finding to the previously published $Ba_2Cd_2Sb_3$ [39] and Ba_2ZnSb_2 [5], for example, in which the Ba atoms, despite their very low electronegativity (χBa = 0.9 on the Pauling scale [30]), also have important contributions to the DOS near the Fermi levels.

Last, we turn our attention to the COHP plots for $Na_{15}Ca_3In_5Sb_{12}$, $Na_4CaGaSb_3$ and $Na_{11}Ca_2Al_3Sb_8$ presented in Figure 1.7. From the graphs, it can be surmised that all In−Sb, Ga−Sb, and Al−Sb interactions are fully optimized at the Fermi level. This is expected because optimization of the interactions (at least within the anionic substructure) is a typical feature of the classic Zintl compounds. Considering the Na−Sb interactions involving the intralayer Na atoms, it becomes obvious that, for both $Na_4CaGaSb_3$ and $Na_{11}Ca_2Al_3Sb_8$, the Na−Sb bonding states are also filled at the Fermi level; i.e., the bonding is again optimized. Compared with the Ga−Sb and Al−Sb COHPs, however, it is noticeable that the Na−Sb interactions are much weaker. For instance, in $Na_4CaGaSb_3$, the integrated COHPs of the Na−Sb bonds (within the Na2 tetrahedra) range from 0.024 to 0.036, more than 5 times smaller than the integrated COHPs of the Ga−Sb bonds, which range from 0.143 to 0.217.

2.5 Conclusions

The three new compounds $Na_{15}Ca_3In_5Sb_{12}$, $Na_4CaGaSb_3$, and $Na_{11}Ca_2Al_3Sb_8$ are the first structurally characterized phases in the respective quaternary Na−Ca−Tr−Sb systems (Tr = Al, Ga, In). Their structures boast different structure types and feature the following: two-dimensional $[InSb_2]$ layers in $Na_{15}Ca_3In_5Sb_{12}$; one-dimensional $[GaSb_3]$ helical chains in $Na_4CaGaSb_3$. In the $Na_{11}Ca_2Al_3Sb_8$ structure, one finds isolated $[Al_3Sb_8]$ trimeric species. All three structures are related to the ubiquitous TiNiSi structure type. The study of the close structural relationships is greatly facilitated by considering some of the Na atoms in ambivalent roles, i.e., as contributing to the covalent bonding and forming complex Na−Al−Sb and Na−Ga−Sb slabs. The computed electronic structures show narrow band gaps at the Fermi level, suggesting that the title compounds could be

considered as Zintl phases. The band gaps open in order of reduced dimensionality on the order from the In to the Ga to the Al compound. The expected intrinsic semiconducting properties could be of relevance to the development of new thermoelectric materials.

Table 2.1. Selected Single-Crystal Data Collection and Structure Refinement Parameters for $Na_{11}Ca_2Al_3Sb_8$, $Na_4CaGaSb_3$, and $Na_{15}Ca_3In_5Sb_{12}$

empirical formula	**$Na_{11}Ca_2Al_3Sb_8$**	**$Na_4CaGaSb_3$**	**$Na_{15}Ca_3In_5Sb_{12}$**
Fw	1387.99	567.01	833.78
Temperature (K)	200 (2)		
radiation, λ (Å)	Mo Kα, 0.71073		
space group	*Pmn2₁* (No.31)	*Pc* (No.7)	*Pmc2₁* (No.26)
Z	2	4	1
a, Å	18.9690(15)	9.1513(9)	4.7609(5)
b, Å	8.8533(7)	8.9852(9)	9.1680(10)
c, Å	7.9304(7)	12.2305(12)	7.8898(8)
β (deg)		97.840(1)	
V, Å^3	1331.8(2)	996.3(2)	344.37(6)
ρ_{cal} (g/cm^3)	3.46	3.78	4.02
μ (cm^{-1})	86.4	113.3	109.6
GOF on F^2	1.051	0.994	1.106
Flack parameter	0.02(4)	0.04(1)	0.08(9)
unique reflns	3716	5260	1058
refined param	119	165	38
R1 [$I > 2\sigma(I)$][b]	0.0288	0.0210	0.0301
wR2 [$I > 2\sigma(I)$][b]	0.0598	0.0411	0.0617

[a]Refined formulas with freely refined occupancies of the Na/Ca mixed positions: $Na_{10.90(2)}Ca_{2.10}Al_3Sb_8$, $Na_{3.98(1)}Ca_{1.02}GaSb_3$, and $Na_{5.06(2)}Ca_{0.94}In_{1.58(2)}Sb_2$, respectively. [b]R1 = $\Sigma||F_o| - |F_c||/\Sigma|F_o|$; wR2 = $[\Sigma[w(F_o^2 - F_c^2)2]/\Sigma[w(F_{o2})^2]]^{1/2}$, where $w = 1/[\sigma^2F_o^2 + (AP)^2 + (BP)]$, and $P = (F_o^2 + 2F_c^2)/3$; *A*, *B* = weight coefficients.

Table 2.2. Atomic Coordinates and Equivalent Isotropic Displacement Parameters U_{eq} a for $Na_{11}Ca_2Al_3Sb_8$

Atom	Wyckoff Site	*x*	*y*	*z*	U_{eq} (Å^2)
Na(1)/Ca(1)[b]	4*b*	0.7560(1)	0.9466(2)	0.9845(2)	0.0254(4)
Na(2)	4*b*	0.8817(2)	0.5935(4)	0.9494(5)	0.0377(7)
Na(3)	4*b*	0.7499(2)	0.6654(3)	0.6288(4)	0.0286(7)
Na(4)	4*b*	0.6307(2)	0.5715(4)	0.9546(4)	0.0341(7)
Na(5)	4*b*	0.6242(1)	0.8027(3)	0.3255(4)	0.0289(7)
Na(6)	2*a*	0	0.9484(4)	0.0000(5)	0.0264(8)
Na(7)	2*a*	0	0.3384(4)	0.1289(6)	0.0285(9)
Ca(2)	2*a*	0	0.0809(2)	0.4897(3)	0.0284(5)
Al(1)	4*b*	0.8772(1)	0.8351(2)	0.3371(3)	0.0207(4)
Al(2)	2*a*	0	0.6862(3)	0.6153(4)	0.0199(6)
Sb(1)	4*b*	0.8852(1)	0.8633(1)	0.6853(1)	0.0208(1)
Sb(2)	4*b*	0.7309(1)	0.3311(1)	0.7350(1)	0.0242(1)
Sb(3)	4*b*	0.6265(2)	0.8778(1)	0.7205(1)	0.0201(1)
Sb(4)	2*a*	0	0.6814(1)	0.2679(1)	0.0197(1)
Sb(5)	2*a*	0	0.4016(1)	0.7268(1)	0.0215(1)

[a]U_{eq} is defined as one-third of the trace of the orthogonalized U_{ij} tensor. [b]Refined freely as 55(1)% Ca and 45% Na; in the final refinement model, for simplicity, constrained to 50% Ca and 50% Na.

Table 2.3. Atomic Coordinates and Equivalent Isotropic Displacement Parameters U_{eq} a for $Na_4CaGaSb_3$

Atom	Wyckoff Site	*x*	*y*	*z*	U_{eq} (Å^2)
Na(1)/Ca(1)[b]	2*a*	0.0000(2)	0.9406(2)	0.0001(1)	0.0207(3)
Na(2)/Ca(2)[b]	2*a*	0.0433(9)	0.1952(8)	0.7189(9)	0.02534
Na(3)	2*a*	0.0847(6)	0.3274(3)	0.4588(7)	0.02111
Na(4)	2*a*	0.1498(1)	0.3966(8)	0.1845(7)	0.02999
Na(5)[c]	2*a*	0.3191(8)	0.0415(4)	0.3287(4)	0.01668
Na(6)	2*a*	0.4302(5)	0.6628(5)	0.2703(9)	0.02928
Na(7)	2*a*	0.4557(6)	0.4075(7)	0.4946(6)	0.01966
Na(8)	2*a*	0.7608(3)	0.3368(9)	0.1042(0)	0.02900
Na(9)	2*a*	0.7978(5)	0.5604(3)	0.3395(0)	0.04733
Ca(3)	2*a*	0.6573(0)	0.0471(7)	0.6549(6)	0.01501
Ga(1)	2*a*	0.4022(8)	0.1745(6)	0.0429(0)	0.01575
Ga(2)	2*a*	0.7230(1)	0.1726(0)	0.3751(6)	0.01561
Sb(1)	2*a*	0.1912(6)	0.6544(2)	0.4329(5)	0.01821
Sb(2)	2*a*	0.3102(6)	0.1063(3)	0.5869(5)	0.01275
Sb(3)	2*a*	0.4988(1)	0.3125(2)	0.2398(9)	0.01684
Sb(4)	2*a*	0.6426(8)	0.1221(6)	0.9169(2)	0.01328
Sb(5)	2*a*	0.7907(7)	0.3350(3)	0.5587(8)	0.01783
Sb(6)	2*a*	0.9570(4)	0.1295(0)	0.2620(7)	0.01315

[a]U_{eq} is defined as one-third of the trace of the orthogonalized U_{ij} tensor. [b]Refined freely as 60(1)% Ca and 40% Na; in the final refinement model, for simplicity, constrained to 60% Ca and 40% Na.

[c]Refined freely as 37(1)% Ca and 63% Na; in the final refinement model, for simplicity, constrained to 40% Ca and 60% Na.

Table 2.4. Atomic Coordinates and Equivalent Isotropic Displacement Parameters U_{eq} a for $Na_{15}Ca_3In_5Sb_{12}$

Atom	Wyckoff Site	*x*	*y*	*z*	U_{eq} (Å^2)
Na(1)	2*b*	1/2	0.4152(5)	0.0489(6)	0.036(1)
Na(2)	2*a*	0	0.3262(5)	0.3630(6)	0.027(1)
Na(3)/Ca(3)[b]	2*a*	0	0.0613(4)	0.0000(4)	0.0215(6)
In	2*b*	1/2	0.1786(1)	0.6558(1)	0.0234(2)
Sb(1)	2*b*	1/2	0.1197(1)	0.2868(1)	0.0180(1)
Sb(2)	2*a*	0	0.6559(8)	0.2618(1)	0.0344(2)

[a]U_{eq} is defined as one-third of the trace of the orthogonalized U_{ij} tensor. [b]Refined freely as 53(1)% Ca and 47% Na; in the final refinement model, for simplicity, constrained to 50% Ca and 50% Na.

Table 2.5. Selected Interatomic Distances (Å) and Angles (deg) in $Na_{11}Ca_2Al_3Sb_8$, $Na_4CaGaSb_3$, and $Na_{15}Ca_3In_5Sb_{12}$

$Na_{11}Ca_2Al_3Sb_8$		**$Na_8Ca_2Ga_2Sb_6$**		**$Na_{15}Ca_3In_5Sb_{12}$**	
Al1–Sb1	2.777 (2)	Ga1–Sb1	2.6812 (7)	In–Sb1	2.924 (1)
Al1–Sb2	2.650 (2)	Ga1–Sb2	2.7374 (7)	In–Sb1	2.961 (1)
Al1–Sb3	2.706 (2)	Ga1–Sb3	2.7461 (7)	In–Sb2 (× 2)	2.9436 (8)
Al1–Sb4	2.753 (2)	Ga1–Sb4	2.8913 (7)	Na2–Sb1	3.101 (3)
Al2–Sb1 (× 2)	2.739 (1)	Ga2–Sb3	2.7568 (7)	Na2–Sb2	3.127 (5)
Al2–Sb4	2.756 (3)	Ga2–Sb4	2.8142 (7)	Na2–Sb2	3.150 (5)
Al2–Sb5	2.670 (3)	Ga2–Sb5	2.6792 (7)		
Na5–Sb1	3.165 (3)	Ga2–Sb6	2.7310 (7)		
Na5–Sb2	3.078 (3)	Na3–Sb1	3.089 (2)		
Na5–Sb3	3.202 (3)	Na3–Sb2	3.207 (2)		
Na5–Sb5	3.071 (3)	Na3–Sb5	3.086 (2)		
Na7–Sb3 (× 2)	3.154 (3)	Na3–Sb6	3.087 (2)		
Na7–Sb4	3.230 (4)				
Na7–Sb5	3.238 (4)				
Sb1–Al1–Sb2	113.44 (7)	Sb1–Ga1–Sb2	114.02 (7)	Sb1–In–Sb1	100.18 (3)
Sb1–Al1–Sb3	104.95 (7)	Sb2–Ga1–Sb3	108.31 (2)	Sb2–In–Sb2	107.94 (4)
Sb1–Al1–Al4	101.32 (7)	Sb3–Ga1–Sb4	111.35 (2)	Sb1–In–Sb2	112.41 (2)
Sb2–Al1–Sb3	113.39 (8)	Sb1–Ga1–Sb4	111.98 (3)	Sb2–In–Sb1	111.93 (2)
Sb2–Al1–Sb4	108.53 (9)	Sb1–Ga1–Sb3	107.74 (6)		
Sb3–Al1–Sb4	114.58 (6)	Sb2–Ga1–Sb4	103.39 (2)		
Sb1–Al2–Sb1	105.45 (2)	Sb3–Ga2–Sb4	110.28 (2)		
Sb1–Al2–Sb4	102.22 (5)	Sb3–Ga2–Sb5	108.83 (2)		
Sb1–Al2–Sb5	118.22 (7)	Sb3–Ga2–Sb6	109.36 (4)		
Sb4–Al2–Sb5	108.22 (6)	Sb4–Ga2–Sb5	113.38 (3)		
		Sb4–Ga2–Sb6	101.58 (4)		
		Sb5–Ga2–Sb6	103.20 (4)		

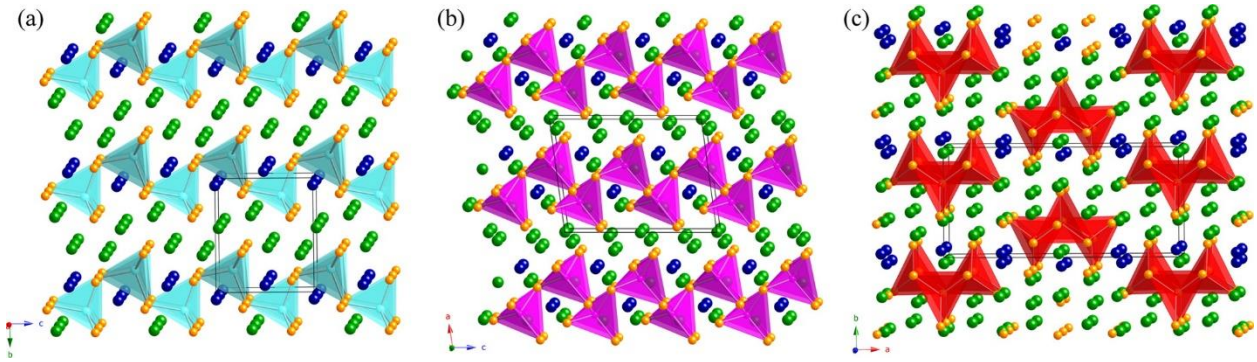

Figure 2.1. Polyhedral views of the structures of $Na_{15}Ca_3In_5Sb_{12}$ (a), $Na_4CaGaSb_3$ (b), and $Na_{11}Ca_2Al_3Sb_8$ (c). The common atom–Ca, Na, and S–are drawn as blue, green, and orange spheres, respectively. The atoms centering the Sb tetrahedra–In, Ga, and Al–are shown in light blue, pink, and red, respectively.

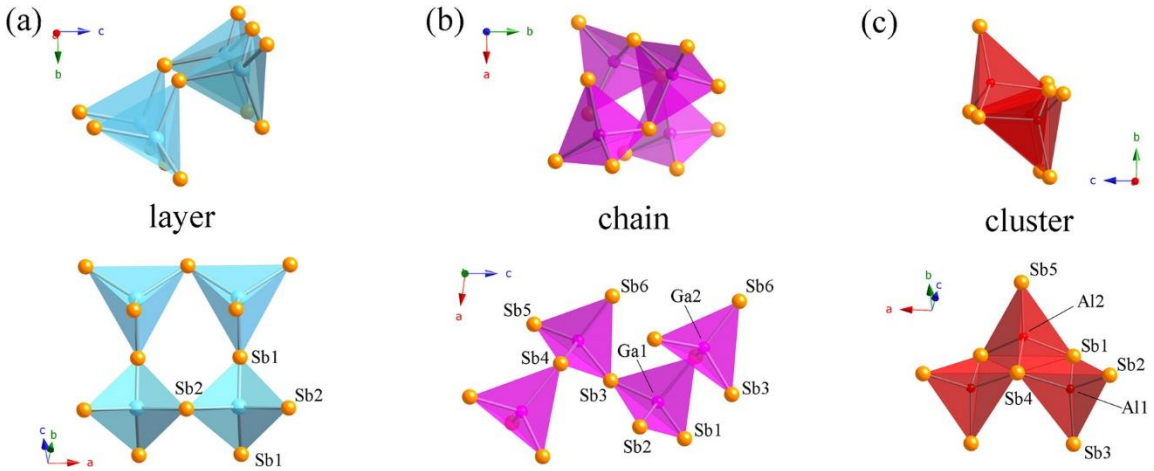

Figure 2.2. Detailed drawings in different orientations of a $[In_4Sb_{12}]$ cutout from the layers of the $Na_{15}Ca_3In_5Sb_{12}$ structure (a), a $[Ga_4Sb_{13}]$ cutout from the chains in the $Na_4CaGaSb_3$ structure (b), and the $[Al_3Sb_8]$ cluster in the $Na_{11}Ca_2Al_3Sb_8$ structure (c). The atoms are labeled, and the relevant distances and angles are listed in Table 1.5.

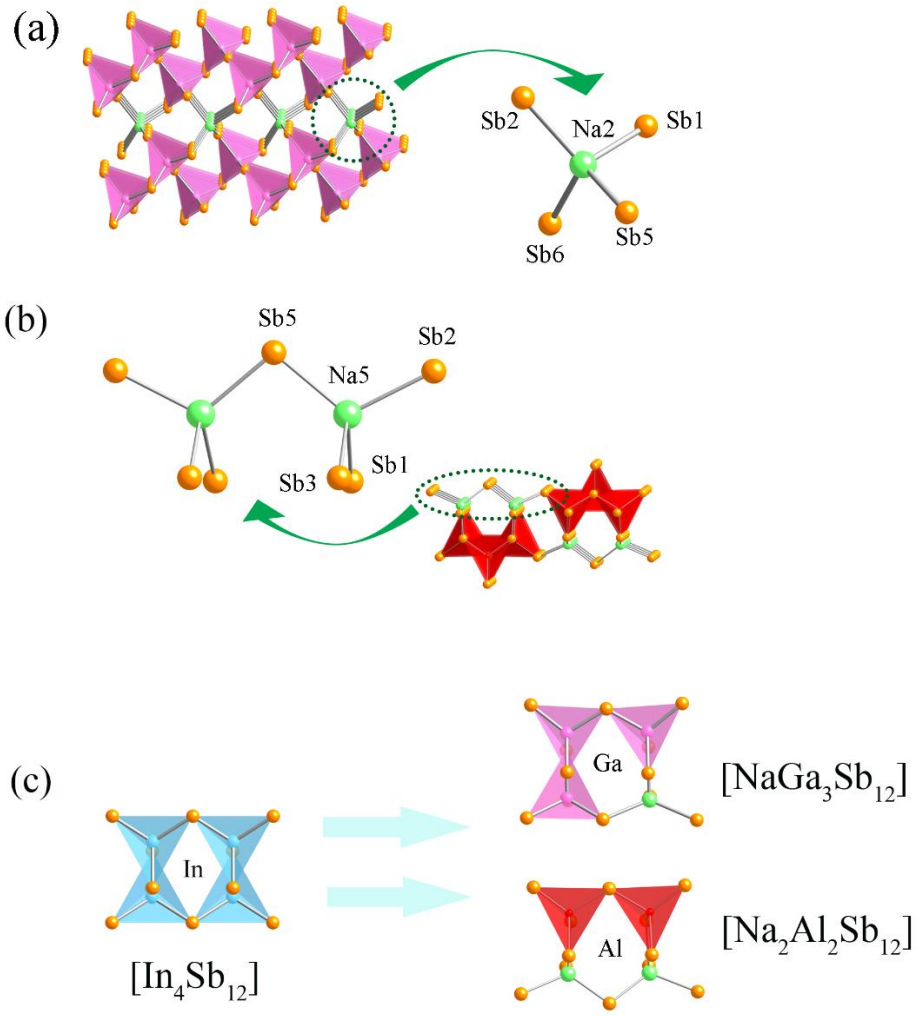

Figure 2.3. Polyanionic substructures of $Na_4CaGaSb_3$ (a) and $Na_{11}Ca_2Al_3Sb_8$ (b) viewed as tetrahedral "hybrid layers", made up of Ga, Na, Sb and Al, Na, Sb, respectively. The atoms are labeled, and the relevant distances are listed in Table 1.5 (c) Structural relationships among $Na_{15}Ca_3In_5Sb_{12}$, $Na_4CaGaSb_3$, and $Na_{11}Ca_2Al_3Sb_8$. Upon closer inspection, one can cut out a $[In_4Sb_{12}]$ subunit from the $[InSb_2]$ layers in $Na_{15}Ca_3In_5Sb_{12}$, and identify the same type of fragment in the "hybrid layers" of the $Na_4CaGaSb_3$ and $Na_{11}Ca_2Al_3Sb_8$ structures. For example, the same type of fragment, which consists of three $GaSb_4$, and one $NaSb_4$ tetrahedra, exist in $Na_4CaGaSb_3$. This subunit can be described as $[Ga_3NaSb_{12}]$. Compared with $[In_4Sb_{12}]$, it is easy to see how one Na atom is replacing one In atom in the subunit structure. Similarly, there are two Na atoms, which together with two Al1 atoms to form the $[Al_2Na_2Sb_{12}]$ subunit in $Na_{11}Ca_2Al_3Sb_8$.

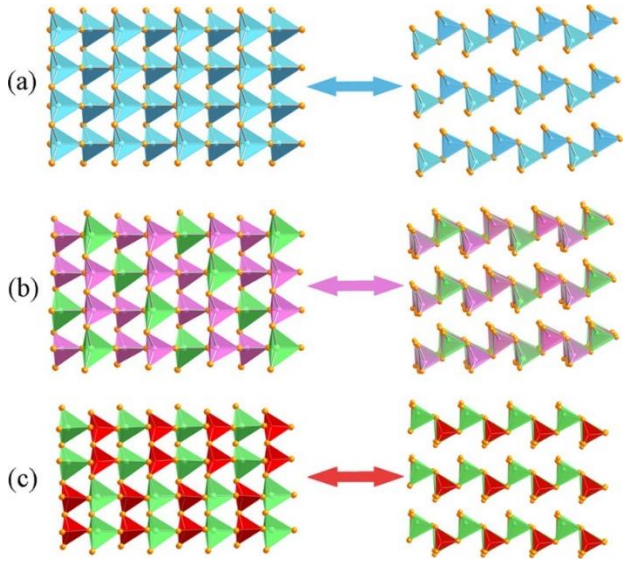

Figure 2.4. Structural relationships among $Na_{15}Ca_3In_5Sb_{12}$, $Na_4CaGaSb_3$, and $Na_{11}Ca_2Al_3Sb_8$. Panel (a) shows the idealized, defect-free $[InSb_2]$ polyanionic layers in $Na_{15}Ca_3In_5Sb_{12}$; panel (b) depicts the hypothetical hybrid $[Ga_{2/3}Na_{1/3}Sb_2]$ layers in $Na_4CaGaSb_3$; panel (c) shows the imaginary $[Al_{1/2}Na_{1/2}Sb_2]$ layers in $Na_{11}Ca_2Al_3Sb_8$. In all drawings, two different orientations are shown, with the tetrahedra rendered in green corresponding to the $NaSb_4$ units.

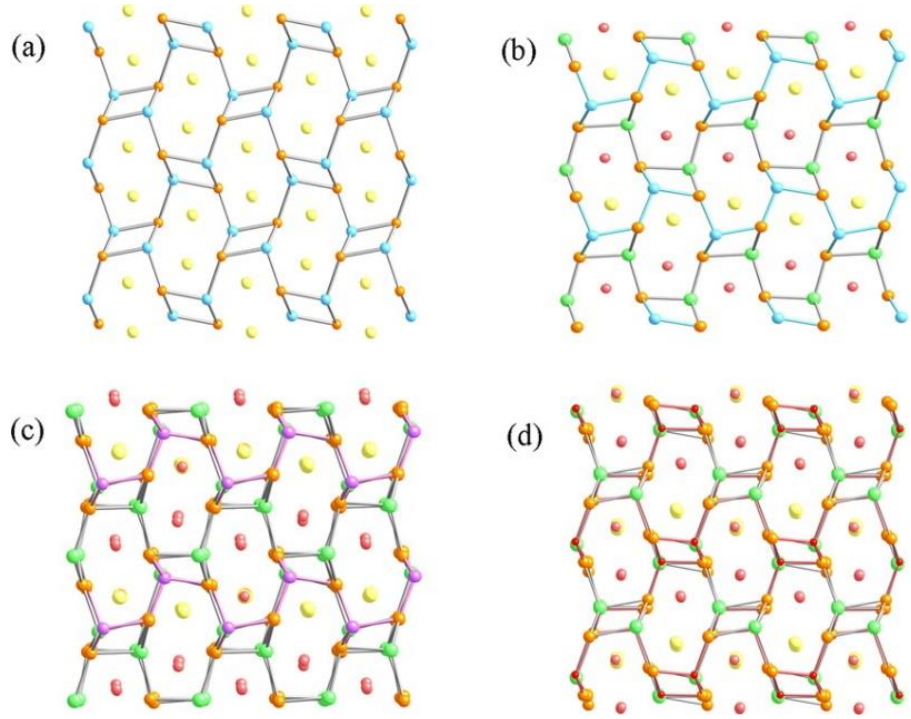

Figure 2.5. Structural relationships among $Na_3In_2Bi_3$ (TiNiSi structure type) [36] and $Na_{15}Ca_3In_5Sb_{12}$, $Na_4CaGaSb_3$, and $Na_{11}Ca_2Al_3Sb_8$. Panel (a) shows the three-dimensional framework of the parent structure with Na shown in yellow, In shown in blue, and Bi shown in orange. Panels (b)−(d) depict the structures of $Na_{15}Ca_3In_5Sb_{12}$, $Na_4CaGaSb_3$, and $Na_{11}Ca_2Al_3Sb_8$, where the frameworks include the tetrahedrally coordinated Na atoms. To guide the eye, the In−Sb, Ga−Sb, and Al−Sb bonds are colored with the respective elemental colors−blue, pink, and red−and the Na−Sb "bonds" are drawn as gray cylinders.

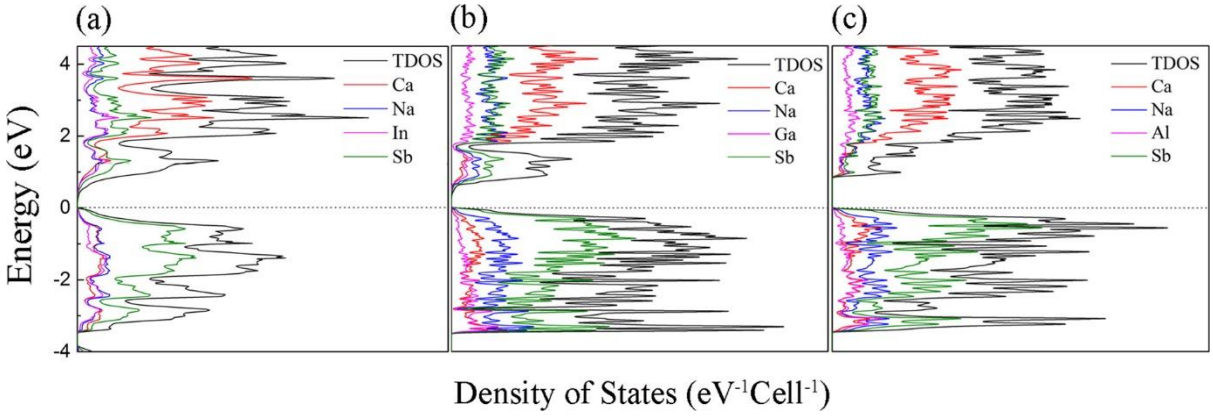

Figure 2.6. Calculated total and partial DOS curves for $Na_{15}Ca_3In_5Sb_{12}$ (a), $Na_4CaGaSb_3$ (b), and $Na_{11}Ca_2Al_3Sb_8$ (c). The Fermi level is the energy reference at 0 eV.

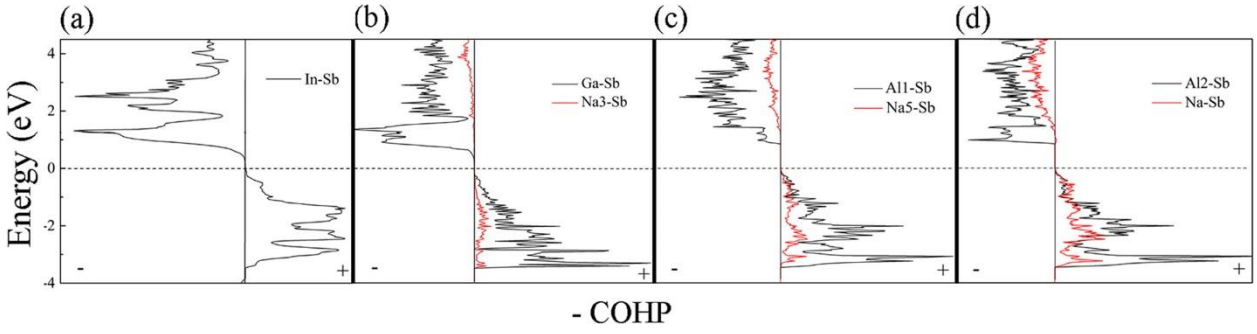

Figure 2.7. COHP curves for In−Sb, Ga−Sb, and Al−Sb (black lines) and for selected Na−Sb interactions (red lines). Panel (a) refers to $Na_{15}Ca_3In_5Sb_{12}$, panel (b) refers to $Na_4CaGaSb_3$, and panels (c) and (d) refer to $Na_{11}Ca_2Al_3Sb_8$. In plots of the COHP curves, the COHP values were inverted (i.e., −COHP is shown) so that the positive and negative regions represent bonding and antibonding states, respectively. The Fermi level is the energy reference at 0 eV.

REFERENCES

1. Schäfer, H.; Eisenmann, B.; Muller, W. *Angew. Chem., Int. Ed. Engl*. **1973**, *12*, 694. (b) Corbett, J. D. *Angew. Chem., Int. Ed.* **2000**, *39*, 670.

2. (a) Kauzlarich, S. M., Ed. Chemistry, Structure and Bonding in Zintl Phases and Ions; VCH: New York, 1998; and references cited therein. (b) Miller, G. J. *Eur. J. Inorg. Chem*. **1998**, 523.

3. Xia, S.-Q.; Bobev, S. *Inorg. Chem*. **2008**, *47*, 1919.

4. Xia, S.-Q.; Bobev, S. *J. Am. Chem. Soc*. **2007**, *129*, 4049.

5. Saparov, B.; Bobev, S. *Inorg. Chem*. **2010**, *49*, 5173.

6. Brown, S. R.; Kauzlarich, S. M.; Gascoin, F.; Snyder, G. J. *Chem. Mater*. **2006**, *18*, 1873.

7. Sales, B. C.; Mandrus, D.; Williams, R. K. *Science*. **1996**, *272*, 1325.

8. Gascoin, F.; Ottensmann, S.; Stark, S.; Haïle, S. M.; Snyder, G. J. *Adv. Funct. Matter*. **2005**, *15*, 1860.

9. Andersen, O. K. *Phys. Rev. B: Condens. Matter*. **1975**, *12*, 3060.

10. Villars, P., Calvert, L. D., Eds. Pearson's Handbook of Crystallographic Data for Intermetallic Compounds, 2nd ed.; American Society for Metals: Materials Park, OH, 1997.

11. Wang, Y.; Bobev, S. Unpublished results.

12. Cordier, G.; Schäfer, H.; Stelter, M. Z. *Naturforsch*. **1985**, *B40*, 5.

13. Cordier, G.; Ochmann, H. Z. *Kristallogr*. **1991**, *195*, 107.

14. Deller, K.; Eisenmann, B. Z. *Naturforsch*. **1976**, *B31*, 29.

15. Cromer, D. T. *Acta Crystallogr*. **1959**, *12*, 41.

16. (a) SMART; Bruker AXS Inc.: Madison, WI, 2003. (b) SAINT; Bruker AXS Inc.: Madison, WI, 2003.

17. SADABS; Bruker AXS Inc.: Madison, WI, 2003.

18. SHEXLTL; Bruker AXS Inc.: Madison, WI, 2003.

19. Jepsen, O.; Burkhardt, A.; Andersen, O. K. The TB-LMTO-ASA Program, version 4.7; Max-Planck Institut für Festkörperforschung: Stuttgart, Germany, 1999.

20. Andersen, O. K.; Jepsen, O. *Phys. Rev. Lett*. **1984**, *53*, 2571.

21. Andersen, O. K.; Pawlowska, Z.; Jepsen, O. *Phys. Rev. B Condens. Matter*. **1986**, *34*, 5253.

22. Dronskowski, R.; Blöchl, *P. E. J. Phys. Chem*. **1993**, *97*, 8617.

23. Barth, U.; Hedin, L. *J. Phys. C: Solid State Phys.* **1972**, *5*, 1629.

24. Andersen, O. K.; Jepsen, O.; Glötzel, D. In Highlights of Condensed Matter Theory; Bassani, F., Fumi, F., Tosi, M., Eds.; North-Holland: New York, **1985**.

25. Blöchl, P. E.; Jepsen, O.; Andersen, O. K. *Phys. Rev. B: Condens. Matter*. **1994**, *49*, 16223.

26. Saparov, B.; Saito, M.; Bobev, S. *J. Solid State Chem*. **2011**, *184*, 432.

27. The one-electron difference between Cd and In, while maintaining an ideal valence electron count, is compensated for by defects on the In site and the concomitant nearly equal cooccupation by Ca and Na on one of the cation sites.

28. Xia, S.-Q.; Bobev, S. *Chem.–Asian J.* **2007**, *2*, 619.

29. Cordier, G.; Schäfer, H.; Stelter, M. Z. *Naturforsch*. **1985**, *B40*, 858.

30. Pauling, L. The Nature of the Chemical Bond; Cornell University Press: Ithaca, NY, **1960**.

31. The integrated COHP values nicely correlate with the bond distances. For example, for the shortest Ga1−Sb1 bond, the integrated COHP value is calculated to be 0.217.

Considering Ga2, the Ga2−Sb5 bond is comparably short and has an integrated COHP value of 0.211. The longer bonds are weaker, and their integrated COHP values are 0.143 for Ga1−Sb4 and 0.160 for Ga2−Sb4.

32. Cordier, G.; Ochmann, H.; Schäfer, H. *Mater. Res. Bull*. **1986**, *21*, 331.

33. ICSD Database; Fachinformationszentrum: Karlsruhe, Germany, **2014**.

34. Cordier, G.; Czech, E.; Jakowski, M.; Schäfer, H. *Rev. Chim*. **1981**, *18*, 9.

35. Cordier, G.; Ochmann, H.; Schäfer, H. Z. *Anorg. Allg. Chem*. **1984**, *517*, 118.

36. Saparov, B.; Xia, S.-Q.; Bobev, S. *Inorg. Chem*. **2008**, *47*, 11237.

37. Saparov, B.; Broda, M.; Ramanujachary, K. V.; Bobev, S. *Polyhedron*. **2010**, *29*, 456.

38. Bobev, S.; Sevov, S. C. *J. Solid State Chem*. **2001**, *163*, 436.

39. Saparov, B.; He, H.; Zhang, X. H.; Greene, R.; Bobev, S. *Dalton Trans*. **2010**, *39*, 1063.

Chapter 3

EFFICIENT TAILORING OF BAND GAP INDUCED BY RARE EARTH (*RE*) METALS DOPING–DETERMINING STRUCTURE AND PROPERTIES OF NARROW–GAP SEMICONDUCTOR $Ca_{9-x}RE_xMn_4Sb_9$ (*RE* = La, Ce, Pr, Nd AND Sm)

3.1 Abstract

A new phase $Ca_{9-x}RE_xMn_4Sb_9$ (*RE* = La, Ce, Pr, Nd and Sm) were synthesized with visible size by flux reaction at high temperature, and their structures have been determined by single-crystal X-ray diffraction. $Ca_{9-x}RE_xMn_4Sb_9$ series crystallize with the primitive orthorhombic space group *Pbam* (No. 55). The structure type could be viewed as "Mn-split" derivative structure from its parent structure $Ca_9Mn_4Bi_9$. Scanning electron microscope (SEM) pictures indicated *RE* metals were successfully doped into the material and the atomic ratio was in good agreement with refined data from single-crystal X-ray diffraction. Compared with poor metallic material $Ca_9Mn_4Bi_9$, electrical resistivity of this series were measured and represented narrow-band gap semiconductive property as expected due to *RE* doping. Temperature-dependent magnetization measurements indicated paramagnetic property at room temperature and suggested Mn^{2+} and Mn^{3+} could co-existed in this structure type. From electron structure calculation, it suggested the structure could optimize itself to rescale the Fermi lever based on the mixed-valence of Mn.

3.2 Introduction

In recent years, intermetallic compounds have acquired a growing importance in many areas of modern chemistry and materials science accounting for diverse structure types and unique physical properties [1-11]. Zintl phases are a subset of intermetallic compounds,

whose structures can be rationalized by assuming complete transfer of valence electrons from the electropositive elements to the electronegative ones so that each element achieves a closed shell configurations [12-15].

Such compounds contained electronegative p-block elements and d-metals, involved directional interactions to form polyanions; whereas more electrostatic interaction existed between cations and polyanions. Therefore this kind of materials are neither covalent nor ionic compounds, which usually exhibite as poor metallic or semi-conductive properties. As we know, doping has been widely performed in materials science, as an efficient way to improve the conductivity of semiconductors by introducing impurities: greatly increasing additional charge carriers into materials [16-24]. Based on Zintl concept and electronic structure, we may rescale the Fermi lever and tailor the band gap by doping, therefore modulating electrical properties of intermetallic compounds.

In an attempt to try out this idea, $Ca_9Mn_4Bi_9$ [25] structure was considered to be appropriate in our exploration. Traced back to 1970s, $Ca_9Mn_4Bi_9$ was first synthesized, and this structure was intensively studied in the last 10 years [26-29]. It was noted that the problem of electron deficiency was considered to be the most important feature of this structure. According to Zintl concept, this structure could be described as $9 \times (Ca^{2+}) + [Mn_4Bi_9]^{19-}$ ($4\times (Mn^{2+}) + 4\times (Bi^{3-}) = 19–$), which had one extra negative charge from $[Mn_4Bi_9]^{19-}$. The electronic structure calculation also correspondingly represented Fermi lever localized at bonding area and the material performed like poor metal [28]. Through optimizing the electronic structure, charge balance was required, indicating one more positive charge need to be provided. Therefore electrical property could be improved. From previous work, it was proposed to solving charge imbalance by introducing more transition

metal atoms in the structure [26]. Trivalent rare earth (*RE*) metals doping is considered here to be another possible way to solve the problem (except divalent Eu and Yb). It's noted replacing one divalent Ca atom with one trivalent *RE* atom, $Ca_8REMn_4Sb_9$ could achieve charge balance in the structure. Therefore, the inclusion of *RE* doping will provide us a new opportunity to study the crystal chemistry, the potential phase width and the physical properties for "9–4–9" system.

Based on the above consideration, $Ca_{9-x}RE_xMn_4Sb_9$ (*RE* = La, Ce, Pr, Nd and Sm) series compounds were successfully synthesized. Here we describe the synthesis by different methods and the byproduct of reactions. Crystal structure is presented and compared with parent structure $Ca_9Mn_4Bi_9$. Electrical resistivity was measured: materials represented narrow band gap semi-conductors as expected. Magnetic susceptibility showed paramagnetic state at room temperature and suggested Mn^{2+} and Mn^{3+} could exist simultaneously in this structure type. In the last paragraph, comparative analysis of electronic structures of related structures were performed.

3.3 Experimental

Synthesis. Calcium and rare earth metals are sensitive to air, therefore all manipulations were carried out in an argon-filled glove box with controlled oxygen and moisture levels below 1ppm, or under vacuum. The metals were purchased from commercial sources and were used as received: rare-earth metals (ingots, 99.9% from Ames Laboratory or Alfa), Ca (Aldrich, granules, 99.9%), Mn (Alfa, pieces, 99.98%), (Sb (Alfa, shot, 99.99%) and Pb (Alfa, granules, 99.999%). The surface of rare-earth metals got cleaned with a blade before shaving into powder.

Two types of reactions were explored: direct reaction and Pb flux reaction. The former one was loaded with stoichiometric mixtures of elements in welded Nb tubes. Then Nb tubes were transferred into fused silica tubes and evacuated until pressure went down below 10^{-3} torr, and the samples were flame-sealed. The mixtures containing starting materials were put into programmable furnace and heated from 373K to 1273K at a rate of 100K/h, then stayed at this temperature for 48h, slowly cooled down to 1073K in 72h, and equilibrated for 96h and cooled down to 773K in 48h and finally cool down to 373K in 12h. The tubes were opened in the glove box and revealed that polycrystalline products were formed from the reaction. The powder X-ray diffraction patterns showed products were not single-phase materials.

In the typical flux reactions, low-melting metal lead was used as a crystal growth medium, and the corresponding elements in the ratio of Ca:*RE*:Mn:Sb:Pb = 3.5:0.5:1.75:4:20 (*RE*= La, Ce, Pr, Nd and Sm) were loaded into 2 cm^3 alumina crucibles. The alumina crucible were then jacketed in fused silica tubes and flame-sealed under a vacuum. The ampoules were put into programmable furnace and heated from 573K to 1273K at a rate of 100K/h, then stayed at this temperature for 48h, slowly cooled down to 1073K in 72h, and equilibrated for 96h and finally cooled down to 773K in 48h. The reactions were taken out and centrifuged to remove Pb flux. The products from all reactions were large needle-shape crystals with some irregular crystals as by-products. The powder X-ray diffraction patterns also showed products were not single-phase materials. However it was easy to pick out our target phase from the product by distinct shapes. Crystals with suitable size were performed on the single-crystal X-ray diffraction experiment and identified as $Ca_{9-x}RE_xMn_4Sb_9$ (*RE*= La, Ce, Pr, Nd and Sm) series compounds. $CaMn_2Sb_2$

was also identified as by-products existing in the synthesis. Control experiment was also made by loading the corresponding elements in the ratio of Ca:Mn:Sb:Pb = 3.5:1.75:4:20. From the reaction, $Ca_9Mn_{4+x}Sb_9$ [29] was found from single-crystal X-ray diffraction.

Powder X-ray Diffraction. The synthesized compounds were ground into fine powder and placed on the holder in the glove box for powder X-ray diffraction experiment. X-ray powder diffraction patterns were taken at room temperature on a Rigaku Miniflex powder diffractometer, using filtered Cu Kα radiation (λ = 1.54056 A). The data were gathered in θ-θ scan mode ($2\theta_{max}$ = 70°) with step-size 0.05° and 1 sec/step counting time. The data were analyzed with the JADE 6.5 software package. It must be noted here, due to the complex structures/large unit cells/low symmetry of title compounds, the diffraction patterns were very complicated. Therefore the powder diffraction patterns were only used for phase identification; single X-ray diffraction data provided all reported cell parameters. The samples were also leave on the bench for several weeks to test the air-sensitivity. According to the powder diffraction patterns, the five title compounds are stable in air for months.

Single-crystal X-ray diffraction. For the intensity data collection on the single-crystal diffractometer, the crystals were picked in the glove box, and cut into desired dimensions under Paratone-N oil. In order to estimate the crystal quality and index unit cell, preliminary rotation images were acquired on a Bruker SMART and APEX 2 CCD-based diffractometer (monochromatized Mo $K\alpha$ radiation, λ=0.71073 A). Full spheres of reciprocal data were also collected with frame width 0.4° in ω at different θ settings. By using cold nitrogen steam, the temperature was kept at 200K during the reaction. The programs *SMART* and *SAINT* [30] was used to acquire and process data. *SADABS* was also

used for the semi-empirical absorption correction [31]. The structures were solved by direct methods, which were refined with the full-matrix least squares on the F^2 method, as implemented in *SHELXTL* [32]. Refined parameters included the scale factor and atomic positions with the corresponding anisotropic displacement parameters. Due to uniformity, before the final refinement steps, the atomic positions were standardized by *STRUCTURE TIDY* [33].

Selected crystallographic information and refinement parameters for $Ca_{8.27}La_{0.73}Mn_4Sb_9$, $Ca_{8.16}Ce_{0.84}Mn_4Sb_9$, $Ca_{8.15}Pr_{0.85}Mn_4Sb_9$, $Ca_{8.11}Nd_{0.89}Mn_4Sb_9$ and $Ca_{7.88}Sm_{1.12}Mn_4Sb_9$ were summarized in Table 2.1-2.5. Final positional and equivalent isotropic displacement parameters were shown in Table 2.6-2.10. Relevant interatomic distances and angles were listed in Table 2.11.

Elemental Analysis. The compositions of $Ca_{8.11}Nd_{0.89}Mn_4Sb_9$ was analyzed with a Hitachi S4700 Scanning Electron Microscope equipped with an INCA-OXFORD energy-dispersive spectrometer (EDS). The beam current was 25 μA at 20 kV accelerating potential, and the counting time for each spot was 240 s. The atomic ratio of different elements was shown as Ca:Nd:Mn:Sb = 38.24:3.39:14.12:44.25, which was very close to the refined composition $Ca_{8.11}Nd_{0.89}Mn_4Sb_9$.

Property Measurement. Field-cooled (FC) direct-current (DC) magnetization measurements on polycrystalline samples were performed in a Quantum Design PPMS. Large needle-shape single-crystals of title compounds were selected under a microscope from freshly prepared samples, and then were ground into powders. Then samples were weighed, loaded in gel capsules and filled with cotton to prevent the material moving under the magnetic field. Material's preparation was done in the glove box, and the filled gel

capsules were immediately transferred to the chamber of PPMS. The raw magnetization data were converted to molar susceptibility of Mn for $Ca_{8.27}La_{0.73}Mn_4Sb_9$ and susceptibility per formula for the other four title compounds. And the net effective moments were calculated from a linear fit of the inverse magnetic susceptibility versus temperature.

By using four probes method, the measurements of electrical resistivity were also done with the PPMS. It was noted that same piece of crystal was cut and used for single crystal X-ray diffraction and electrical resistivity measurement. The sample size of title compounds was around 0.5mm ×0.5mm ×1mm. The crystals were connected to the holder by four platinum with silver epoxy. The measurement was carried out from 5K to 300K with excitation current of 10 mA and to ensure reproducibility, measurements were taken twice on heating and cooling. Band gap was calculated from a linear fit of $ln\rho$ (1/T) plot.

3.4 Results and Discussion

Characterization. The five title compounds $Ca_{9-x}RE_xMn_4Sb_9$ (RE = La, Ce, Pr, Nd and Sm) were successfully synthesized in a large amount from flux reactions at high temperature. Figure 2.1a shows the optical microscope image of $Ca_{8.11}Nd_{0.89}Mn_4Sb_9$, from which it was obvious that crystals are opaque and black, and have average size (around 2 mm × 0.5 mm × 0.5 mm).

Figure 2.1b and 2.1c shows the scanning electron microscope (SEM) pictures with the scale bar at 300μm and 5μm respectively. Figure 2.1b shows the overall view of needle-shape crystals under scanning electron microscope. From Figure 2.1c, there were several strips on the crystal surface, which maybe result from disorder in the crystal like twinning. In order to better investigate the type of disorder and identify the interplanar spacings of

the crystal lattices, high-resolution transmission electron microscope (HRTEM) was required for further work. Energy dispersive X-ray analysis (EDS) was performed from the squared area in order to obtain complementary information on the crystal composition. The atomic ratio of different elements is calculated to be Ca:Nd:Mn:Sb = 38.24:3.39:14.12:44.25, which is very close to the refined composition $Ca_{8.11}Nd_{0.89}Mn_4Sb_9$.

Single-crystal X-ray Diffraction was also used to determinate the structure and composition of the title compounds. Important crystallographic data for $Ca_{9-x}RE_xMn_4Sb_9$ (*RE* = La, Ce, Pr, Nd and Sm) were shown in Table 2.1–2.5. Trends of unit cell constants of title compounds were investigated: from Figure 2.2a it was pronounced that unit cell constants were reduced from $Ca_{8.27}La_{0.73}Mn_4Sb_9$ to $Ca_{7.88}Sm_{1.12}Mn_4Sb_9$ because of lanthanide contraction, which also provided another evidence of the success of *RE* doping in our materials. Doping amount of *RE* metals of the title compounds was also studied. According to single-crystal X-ray refinement, it was worth noting here that the doping amount of *RE* metals was around one per formula, which was close to our target compounds $Ca_8REMn_4Sb_9$ and generally increased from $Ca_{8.27}La_{0.73}Mn_4Sb_9$ (La=0.73) to $Ca_{7.88}Sm_{1.12}Mn_4Sb_9$ (Sm=1.12) (Figure 2.2b black column). Lanthanide contraction could be considered to be the possible reason. Tables 2.6–2.10 show atomic coordinates and equivalent isotropic displacement parameters for title compounds. It is noticeable that disorder exists: compared with parent structure, there was an extra position of Mn3 split from Mn2. It was interesting that split percentage of Mn3 decreased from $Ca_{8.27}La_{0.73}Mn_4Sb_9$ (19.5%) to $Ca_{7.88}Sm_{1.12}Mn_4Sb_9$ (11.3%) (Figure 2b red column), inversely proportional to the doping amount. More details of the reason will be discussed in structure part.

Structure and Bonding. This structure type is similar to its parent structure type $Ca_9Mn_4Bi_9$, which has already been discussed in previous paper [25], therefore only a brief description about *RE* doped structure was provided below. Inspection would be focused on the difference between $Ca_9Mn_4Bi_9$ and $Ca_{9-x}RE_xMn_4Sb_9$ to illustrate the structure relationship between these two structures. And investigation on bonding distances and corresponding angles would provide more details in order to fully understand *RE* doped structure type. Further study between $Ca_{8.27}La_{0.73}Mn_4Sb_9$ and $Ca_{7.88}Sm_{1.12}Mn_4Sb_9$ represented proper explanation for reducing tendency of split percentage of Mn3 in the series.

The five new quaternary compounds $Ca_{8.27}La_{0.73}Mn_4Sb_9$, $Ca_{8.16}Ce_{0.84}Mn_4Sb_9$, $Ca_{8.15}Pr_{0.85}Mn_4Sb_9$, $Ca_{8.11}Nd_{0.89}Mn_4Sb_9$ and $Ca_{7.88}Sm_{1.12}Mn_4Sb_9$ were crystalized in a new structure type with the orthorhombic space *Pbam* (No. 55). There were total 13 crystallographic sites in the asymmetric unit: 5 for Ca and/or La atoms, 3 for Mn atoms and 5 for Sb atoms, all of which were in special positions with z = 0 or z =1/2. The structure was depicted in Figure 2.3. The most remarkable point was that in the *RE* doped structure, there were three Mn sties, compared with two sites of Mn in its parent structure $Ca_9Mn_4Bi_9$. From the refinement, the extra Mn position in *RE* doped structure was Mn3, which split from Mn2 with the ratio from 19.5% (La) reduced to 11.3% (Sm) in the series (Figure 2.2b).

To better illustrate the difference between *RE* doped and its parent structures, the unit cell axes and the nomenclature for the atomic positions were assigned accordingly. Figure 2.4a showed the $Ca_9Mn_4Bi_9$ parent structure, from which we could easily find the characteristic tetrameric $^1_\infty[Mn_4Sb_9]^{-19}$ layers shown as the green parts [28]. In Figure 2.4b, the extra Mn3 positions in the *RE* doped structure are represented as pink tetrahedra.

Combined Figure 2.4a and Figure 2.4b, Figure 2.4c shows the panorama of the *RE* doped structure, which could be considered as "Mn-split" derivative structure from its parent structure. Investigation of Figure 4c suggested that there were two different tetrameric $^{1}_{\infty}[Mn_4Sb_9]^{-19}$ ribbons existing in the *RE* doped structure: original one as seen in Figure 2.4a, which consisted of Mn1 and Mn2 cornered-shared tetrahedra; whereas the other one contained Mn1 and Mn3 shown in Figure 2d as green-pink polyanion network in Figure 2.4d.

To further understand this "Mn-split" derivative structure, more details were investigated. In Figure 2.5, the structure could be also visualized as containing two Mn tetrahedral layers: layer 1 and layer 2 (Figure 2.5a). Layer 1 was build up by Mn2 (yellow) and Mn3 (pink) tetrahedra, while layer 2 consisted of only Mn1 tetrahedra. Compared with Figure 2.4a, it indicates layer 2 has same polyanion network. However due to the splitting of Mn2, Mn3 co-existed with Mn2 in layer 1, and the typical fragment represented in Figure 2.5b. When just considering the original site of Mn2 and Mn1, it established the parent structure, showing typical tetrameric $^{1}_{\infty}[Mn_4Sb_9]^{-19}$ fragments (Figure 2.5c). Inspecting Mn3 atoms, which could be viewed as Mn2 flipping over up and/or down, they connected to adjacent Mn1 layers and rearranged the tetrameric $^{1}_{\infty}[Mn_4Sb_9]^{-19}$ fragments (Figure 2.5d). Investigation on bond distances of $MnSb_4$ tetrahedra showed the Mn–Sb distances varied from 2.7303 Å to 3.009 Å and these values were in good agreement with the sum of the respective Pauling covalent radii [34] ($r_{Mn} + r_{Sb}$ = 2.57 Å), which implied considerable covalent bonding character of the interactions within these polyanions. The corresponding angles for all Mn positions deviated differently from the ideal tetrahedral value of 109.5°, ranging from 99.55(5)° to 115.7(2)°. The numerical values for the lengths of the Mn–Sb

bonds and the Sb−Mn−Sb angles compared well with those reported for other tetrnary *A*MnSb (A = alkaline earth elements) structures, such as $CaMn_2Sb_2$, $Ca_{14}MnSb_{11}$ and $Sr_{21}Mn_4Sb_{18}$ [35-37]. It was worth noting that Mn2 and Mn3 were more distorted than Mn1 as a consequence of disorder. For instance, Mn−Sb bond distances for Mn1 ranged from 2.756(1) Å to 2.850(1) Å; while observation of Mn2 and Mn3 showed that Mn−Sb bond distances were from 2.742(1) Å to 2.905(1) Å and from 2.730(1) Å to 3.009(7) Å respectively. Considering Sb−Mn−Sb angles, it was also indicated layer 1 (Mn2 and Mn3) had more distortion than layer 2 (Mn1). Compared with Mn1, angles of which ranged from 102.11(4)° to 114.92(3)°, Mn2 and Mn3 were from 99.55(5)° to 114.87(6)° and from 99.6(1)° to 115.7(2)° respectively.

Turning back our inspection to Figure 2.5a, we could visualize the structure as layer 1 playing a role like bridge, which shared corners with Mn1 tetrahedra through Sb5 atoms (Figure 2.5e). It is interesting that Sb5 is at a special position because Mn−Sb5 bond distances are the longest ones in both Mn2 and Mn3 tetrahedra, which were 2.905(1) Å and 3.009(7) Å respectively. As we discussed above, Mn2 and Mn3 tetrahedra are highly distorted and specially on Sb5 atoms, which indicated the bridge subunit was not stable and supposed to be very sensitive to the chemical environment. From Figure 2.5e, it is noticeable that Ca2/La2 and Ca4/La4 are very close to the Mn2 and Mn3 atoms. In our previous papers [38, 39], we studied the cation's influence of determining the structural preference. Therefore we also needed to consider the cation's influence in this structure. Compared with other Ca positions, it was pronounced that Ca2 and Ca4 were highly mixed with La atoms, in which the co-occupancy of La atoms were 16.5% and 12.3% respectively.

The co-occupancy of *RE* metals could be the most possible reason why Mn2 split into two positions in the doped structure.

The last point was that the split of Mn3 varied from $Ca_{8.27}La_{0.73}Mn_4Sb_9$ to $Ca_{7.88}Sm_{1.12}Mn_4Sb_9$. As we discussed before, Figure 2.2b represented that percentage of split Mn3 generally reduced from 19.5% (La) to 11.3% (Sm). In order to explore the reason, comparison had been down between these two compounds. On one hand, based on lanthanide contraction, parameters of unit cell generally decreased from $Ca_{8.27}La_{0.73}Mn_4Sb_9$ to $Ca_{7.88}Sm_{1.12}Mn_4Sb_9$. On the other hand, the corresponding doping amount of *RE* metals increases. According to the above two points, bond distances of Mn−Sb are supposed to smoothly decrease from La containing compound to Sm containing compound. The above supposition can be proven by the data in Table 2.7. For instance, all Mn−Sb bond distances for Mn1 and Mn2 in $Ca_{8.27}La_{0.73}Mn_4Sb_9$ are slightly longer than in $Ca_{7.88}Sm_{1.12}Mn_4Sb_9$. It is remarkable that the only exception is the Mn3−Sb5 bond, which is 3.04(1) Å in $Ca_{7.88}Sm_{1.12}Mn_4Sb_9$, compared with 3.009(7) Å in $Ca_{8.27}La_{0.73}Mn_4Sb_9$. It is obvious that Mn3 centered $MnSb_4$ tetrahedra is more distorted and less stable in $Ca_{7.88}Sm_{1.12}Mn_4Sb_9$. As a consequence, probability of existence of Mn3 in $Ca_{7.88}Sm_{1.12}Mn_4Sb_9$ is less than in $Ca_{8.27}La_{0.73}Mn_4Sb_9$, which correlated with the split of Mn3 reducing from $Ca_{8.27}La_{0.73}Mn_4Sb_9$ to $Ca_{7.88}Sm_{1.12}Mn_4Sb_9$.

Physical Properties. The magnetic susceptibility of all compounds have been measured in the temperature ranging from 5K to 300K. In Figure 2.6, at higher temperature, the magnetic behavior of the title compounds appeared to be paramagnetic, which was evidenced by the inverse susceptibility of this series compounds versus temperature plots, together with a linear fit (inset), indicating Curie-Weiss type behavior in the high

temperature. The Curie-Weiss law is $\chi(T) = C/(T - \theta_P)$ [40], where C was the Curie constant, θ_P was the Weiss temperature. From the measurement, the effective magnetic moments were obtained by using $\mu_{eff} = \sqrt{7.99C}\ \mu_B$ (For $Ca_{8.27}La_{0.73}Mn_4Sb_9$, μ_{eff} was based on Mn atoms due to no unpaired electrons in La 4*f* orbitals; for the other four *RE* doped compounds, μ_{eff} was calculated per formula, which was total effective moment, combining *RE* and Mn together). Expected values were calculated by $\mu_{eff} = \sqrt{N_{RE^{3+}}\mu^2_{RE^{3+}} + N_{Mn^{2+}}\mu^2_{Mn^{2+}}}\ \mu_B$ [41], which were compared with the measured effective moments in Table 2.12. It was noted that from $Ca_{8.27}La_{0.73}Mn_4Sb_9$ to $Ca_{7.88}Sm_{1.12}Mn_4Sb_9$, effective moments generally increased from 4.89 μ_B to 11.87 μ_B, one of the obvious reason was more electrons in 4*f* orbitals of rare-earth elements [40] ($\mu_{eff\ Mn}{}^{2+} = 5.92\mu_B$, $\mu_{eff\ Ce}{}^{3+} = 2.54\mu_B$, $\mu_{eff\ Pr}{}^{3+} = 3.58\mu_B$, $\mu_{eff\ Nd}{}^{3+} = 3.62\mu_B$ and $\mu_{eff\ Sm}{}^{3+} = 0.84\mu_B$).

Investigation of the calculated data, suggests that Nd containing compound and Sm containing compound are in good agreement with expected values. However obvious differences are represented from the other three compounds. Here mixed-valent Mn should be considered as a possible reason. The study of mixed-valent compounds has a long history, especially on the investigation of compounds of transition metals [42]. For example, mixed-valent copper-based oxides $YBa_2Cu_3O_7$ has mixed-valent Cu^{2+} and Cu^{3+}, which has been widely known as a superconductor [43]. A number of rare-earth compounds also have shown very unique thermal and magnetic properties. For example, in "9–4–9" system, $Yb_9Zn_4Bi_9$ has been rationalized as $8\times(Yb^{2+})+(Yb^{3+})+[Zn_4Bi_9]^{19-}$ as a mixed-valent Yb system to achieve charge balance [44]. In *RE* doped compounds, considering doping amount of *RE* metals, it was obvious that Nd containing compound and

Sm containing compound were close to idea condition, which was supposed to be one, indicating Mn^{2+} ions existed in the compound to achieve charge balance. Inspecting on the other three compounds, shows that doping amount of *RE* are lower than expected value. Because of the less amount *RE*, less positive charge is provided from the cations, which could force part of the Mn atoms to switch from Mn^{2+} to Mn^{3+} state in order to provide a charge balance. The phenomenon of mixed-valence of Mn in this series can also be evidenced by electrical resistivity measurement, which would be discussed below.

Due to air stability of title compounds, reliable resistivity data as a function of temperature were obtained on single crystals for all compounds. From Figure 2.7, it is remarkable that from ρ(T) plots, resistivity at room temperature was low, which slowly increased with the decreasing temperature, indicating a semi-conductive dependence. From $ln\rho$(1/T) plots (inset), it was apparent that $ln\rho$ increased linearly with 1/T, calculation from which indicated the derived band gap was small, ranging from 0.006eV to 0.440eV. All data suggested title compounds were semi-conductors. $Ca_9Mn_4Bi_9$ performed as poor metal, which proved through designed *RE* doping, we successfully synthesized new materials and impacted the electrical conductivity in a rational and predictable way.

However, it was noted that the ideal situation was $Ca_8REMn_4Sb_9$, which were supposed to be narrow band gap semiconductor and consistent with the measurement as we discussed before. Compared with our refined data (Table 2.1–2.5), it is noticeable that title compounds are not under ideal condition, but still represent narrow band gap semi-conductors. This concern provided more evidence for mixed-valent Mn as discussed previously. From La containing compound to Nd containing compound, *RE* doping was less than one thus introduced negative charge when we considered only Mn^{2+} existing in

the structure. From magnetic susceptibility measurement, it was discovered Mn^{3+} ions co-existed in the structure, which could support the structure to achieve charge balance by reducing negative charge from polyanoin. This hypothesis was proved by resistivity data, which represented excellent narrow band gap semi-conductive property for these four compounds. However, compared with the others, it was remarkable that Sm had a relative higher resistivity 41Ω·m at room temperature, together with a corresponding much larger band gap 0.440eV. It was understandable that from magnetic effective moment discussion, only Mn^{2+} existed in Sm structure and together with more than one mole Sm doped per formula, which produced extra positive charge in the structure, deviating the compound from the idea model. Therefore unlike the other four compounds, Sm containing compound performed slightly differently in electrical resistivity measurement. By elicitation from propertied discussion, it inspired us to investigate electronic structure in order to deeply understand the structure, electronic tuning and width of phase.

Electronic Structure. Depending on our *RE* doped structure, it was hard to directly calculate its electronic structure. Through studying relative "9–4–9" structure types, it would provide a sight of our structure. Investigation of "9–4–9" parent structure showed it could be accounted as $8\times Ca + [Mn_4Bi_9]^{-19}$, which revealed a charge imbalance due to one more electron from $[Mn_4Bi_9]^{-19}$. Calculation had been done on "9–4–9", which confirmed that depending on electron deficiency, the Fermi lever was localized at banding area, suggesting metallic resistivity. Compared with "9–4–9" structure type, studying on another related structure $Yb_9Zn_{4+x}Sb_9$ and $Ca_9Zn_{4+x}Sb_9$ [27] provided a new inspection, which had additional one electron from extra Zn to achieve charge balance. The calculation proved the bonding optimized and system was stabilized with 72 electrons compared with 71

electrons in "9–4–9" parent structure, which indicated there zinc analogs were expected to be a narrow-gap semiconductor.

According to this idea, comparison between "9–4+X–9" and "9-X–X–4–9" would be helpful for us to investigate electronic structure of title compounds. For instance, $Ca_9Zn_{4.5}Sb_9$ [27] could be viewed as one more electron provided by extra Zn from polyanion. Considering $Ca_{9-x}RE_xMn_4Sb_9$, if X equals exactly 1, one more electron was provided from RE^{3+} ions, which also suggested Zintl phase compounds and achieved bonding optimization with 72 electrons. Contrasting to the ideal situation, if X was not exactly 1 and Mn was supposed to be divalent as Cd^{2+}, a little of electron deficient displayed, resulting in Fermi lever moving back down to bonding area; whereas poor metal behavior would be performed. While based on our electrical resistivity measurement, narrow band gap good semiconductors were represented.

Based on new provided evidence, more inspection was required to consider the "9–4–9" structure system with a new insight on the phase width, the bonding, and the chemical environment. A long time ago, it has been suggested that based on the inadequacy of Zintl phase concept, polyanion network would automatically satisfy the charge requirement from cation to achieve balance. There was no electron deficiency existing in the structures, which was evidenced by resistivity measurement. Looking back to magnetic susceptibity, it suggested not only divalent but also trivalent Mn co-existed to balance the positive charge of cations. Therefore depending on the self-optimized requirement in the structure, polyanion would automatically perform electronic tuning of Mn valence states to achieve charge balance and bonding optimization with 72 electrons.

3.5 Conclusions

$Ca_{9-x}RE_xMn_4Sb_9$ (*RE* = La, Ce, Pr, Nd and Sm) have been successfully synthesized and characterized. Scanning electron microscope (SEM) pictures agreed with refinement from single-crystal X-ray diffraction, which suggested *RE* metals doped into the materials. The structure would be visualized as "Mn split" derivative structure from its parent structure $Ca_9Mn_4Bi_9$ with featured $^1_\infty[Mn_4Sb_9]^{-19}$ polyanion subunit. The doping amount of *RE* metals generally increased from $Ca_{8.27}La_{0.73}Mn_4Sb_9$ (La=0.72) to $Ca_{7.88}Sm_{1.12}Mn_4Sb_9$ (Sm=1.12); however percentage of split Mn3 decreased from 19.5% (La) to 11.3% (Sm). Our study suggested cation influence played an important role and determined the structural preference.

Electronic resistivity represented narrow band gap semi-conductive property as expected, which suggested by doping with *RE* metals, Fermi lever was rescaled into gap area. Magnetic susceptibility showed depending on total electron counting, Mn^{2+} and Mn^{3+} could exist simultaneously in this structure type. Considering the connection among measurements, electron structure calculation indicated the structure could optimize itself to tailor the band gap based on the mixed valence of Mn atoms.

Table 3.1. Selected Crystal Data and Structure Refinement Parameters for $Ca_{8.27}La_{0.73}Mn_4Sb_9$,

empirical formula	**$Ca_{8.27}La_{0.73}Mn_4Sb_9$**
Fw	1748.38
Temperature (K)	200(2)
λ, Å	Mo Kα, 0.71073
space group	*P bam* (No. 55)
Z	2
a, Å	12.4552 (9)
b, Å	22.1000 (15)
c, Å	4.6212 (3)
V, $Å^3$	1272.03 (15)
ρ_{calc}, g/cm^3	4.565
μ (Mo *K*α), mm^{-1}	14.138
GOF on F^2	1.042
unique reflns	1469
Refined param	76
R1 $[I > 2\sigma(I)]^a$	0.0241
wR2 $[I > 2\sigma(I)]^a$	0.0505

$^aR1 = \Sigma||F_o| - |F_c||/\Sigma|F_o|$; $wR_2 = [\Sigma [w(F_o^2 - F_c^2)^2]/\Sigma [w(F_o^2)^2]]^{1/2}$, where $w = 1/[\sigma^2F_o^2 + (0.0291P)^2 + 25.6115P]$ and $P = (F_o^2 + 2F_c^2)/3$.

Table 3.2. Selected Crystal Data and Structure Refinement Parameters for $Ca_{8.16}Ce_{0.84}Mn_4Sb_9$

empirical formula	$Ca_{8.16}Ce_{0.84}Mn_4Sb_9$
Fw	1759.76
Temperature (K)	200(2)
λ, Å	0.71073
space group	*P bam* (No. 55)
Z	2
a, Å	12.4347 (6)
b, Å	22.0664(10)
c, Å	4.6189(2)
V, $Å^3$	1267.38(10)
ρ_{calc}, g/cm^3	4.611
μ (Mo *K*α), mm^{-1}	14.433
GOF on F^2	1.102
unique reflns	1460
Refined param	77
R1 $[I > 2\sigma(I)]^a$	0.0205
wR2 $[I > 2\sigma(I)]^a$	0.0457

$^a R1 = \Sigma||F_o| - |F_c||/\Sigma|F_o|$; $wR_2 = [\Sigma [w(F_o^2 - F_c^2)^2]/\Sigma [w(F_o^2)^2]]^{1/2}$, where

$w = 1/[\sigma^2F_o^2 + (0.0183P)^2 + 18.5581P]$ and $P = (F_o^2 + 2F_c^2)/3$.

Table 3.3. Selected Crystal Data and Structure Refinement Parameters for $Ca_{8.15}Pr_{0.85}Mn_4Sb_9$

empirical formula	$Ca_{8.15}Pr_{0.85}Mn_4Sb_9$
Fw	1761.94
T, K	200(2)
λ, Å	0.71073
space group	*P bam* (No. 55)
Z	2
T, K	200(2)
a, Å	12.4143(11)
b, Å	22.059(2)
c, Å	4.6139(4)
V, $Å^3$	1263.5(2)
ρ_{calc}, g/cm^3	4.631
μ (Mo *K*α), mm^{-1}	14.608
GOF on F^2	1.051
unique reflns	1457
Refined param	77
R1 $[I > 2\sigma(I)]^a$	0.0279
wR2 $[I > 2\sigma(I)]^a$	0.0576

$^a R1 = \Sigma||F_o| - |F_c||/\Sigma|F_o|$; $wR_2 = [\Sigma\,[w(F_o^2 - F_c^2)^2]/\Sigma\,[w(F_o^2)^2]]^{1/2}$, where

$w = 1/[\sigma^2F_o^2 + (0.0183P)^2 + 18.5581P]$ and $P = (F_o^2 + 2F_c^2)/3$.

Table 3.4. Selected Crystal Data and Structure Refinement Parameters for $Ca_{8.11}Nd_{0.89}Mn_4Sb_9$

empirical formula	$Ca_{8.11}Nd_{0.89}Mn_4Sb_9$
Fw	1768.93
T, K	200(2)
λ, Å	0.71073
space group	*P bam* (No. 55)
Z	2
a, Å	12.4062(9)
b, Å	22.0551(15)
c, Å	4.6120(3)
V, $Å^3$	1261.94(15)
ρ_{calc}, g/cm^3	4.655
μ (Mo *K*α), mm^{-1}	14.807
GOF on F^2	1.096
unique reflns	1456
Refined param	77
R1 [$I > 2\sigma(I)$][a]	0.0242
wR2 [$I > 2\sigma(I)$][a]	0.0532

[a]$R1 = \Sigma||F_o| - |F_c||/\Sigma|F_o|$; $wR_2 = [\Sigma [w(F_o^2 - F_c^2)^2]/\Sigma [w(F_o^2)^2]]^{1/2}$, where

$w = 1/[\sigma^2F_o^2 + (0.0183P)^2 + 18.5581P]$ and $P = (F_o^2 + 2F_c^2)/3$.

Table 3.5. Selected Crystal Data and Structure Refinement Parameters for $Ca_{7.88}Sm_{1.12}Mn_4Sb_9$

empirical formula	$Ca_{7.88}Sm_{1.12}Mn_4Sb_9$
Fw	1799.73
T, K	200(2)
λ, Å	0.71073
space group	*P bam* (No. 55)
Z	2
a, Å	12.3883(5)
b, Å	22.0164(10)
c, Å	4.6077(2)
V, Å^3	1256.73(9)
ρ_{calc}, g/cm^3	4.756
μ (Mo *K*α), mm^{-1}	15.589
GOF on F^2	1.055
unique reflns	1452
Refined param	77
R1 [I > 2σ(I)][a]	0.0244
wR2 [I > 2σ(I)][a]	0.0535

[a]$R1 = \Sigma||F_o| - |F_c||/\Sigma|F_o|$; $wR_2 = [\Sigma [w(F_o^2 - F_c^2)^2]/\Sigma [w(F_o^2)^2]]^{1/2}$, where

$w = 1/[\sigma^2F_o^2 + (0.0183P)^2 + 18.5581P]$ and $P = (F_o^2 + 2F_c^2)/3$.

Table 3.6. Atomic Coordinates and Equivalent Isotropic Displacement Parameters (U_{eq}[a]) for $Ca_{8.27}La_{0.73}Mn_4Sb_9$

Atom	Wyckoff Site	*x*	*y*	*z*	U_{eq} (Å^2)
A(1)[b]	2*a*	0	0	0	0.014(1)
A(2)[c]	4*h*	0.3604(1)	0.3602(1)	1/2	0.022(1)
A(3)[d]	4*h*	0.0522(1)	0.4079(1)	1/2	0.014(1)
A(4)[e]	4*h*	0.1194(1)	0.2364(1)	1/2	0.016(1)
Ca(5)	4*g*	0.2777(1)	0.1031(1)	0	0.011(1)
Mn(1)	4*g*	0.2150(1)	0.4559(1)	0	0.013(1)
Mn(2)	4*g*	0.3778(1)	0.2588(1)	0	0.013(1)
Mn(3)	4*g*	0.4680(5)	0.2281(3)	0	0.013(1)
Sb(1)	2*c*	0	1/2	0	0.0114(1)
Sb(2)	4*h*	0.1945(1)	0.0021(1)	1/2	0.0128(1)
Sb(3)	4*h*	0.3703(1)	0.1922(1)	1/2	0.0123(1)
Sb(4)	4*g*	0.0340(1)	0.1487(1)	0	0.0105(1)
Sb(5)	4*g*	0.1846(1)	0.3324(1)	0	0.0099(1)

[a]U_{eq} is defined as one-third of the trace of the orthogonalized U_{ij} tensor. [b]Mixed-occupied Ca/La site, refined freely as 92(1)% Ca and 8% La. [c]Mixed-occupied Ca/La site, refined freely as 82(1)% Ca and 17% La. [d]Mixed-occupied Ca/La site, refined freely as 94(1)% Ca and 6% La. [e]Mixed-occupied Ca/La site, refined freely as 87(1)% Ca and 13% La.

Table 3.7. Atomic Coordinates and Equivalent Isotropic Displacement Parameters (U_{eq}[a]) for $Ca_{8.16}Ce_{0.84}Mn_4Sb_9$

Atom	Wyckoff Site	*x*	*y*	*z*	U_{eq} (Å^2)
A(1)[b]	2*a*	0	0	0	0.0138(7)
A(2)[c]	4*h*	0.36124(7)	0.36073(5)	1/2	0.0197(4)
A(3)[d]	4*h*	0.0537(1)	0.40806(5)	1/2	0.0146(5)
A(4)[e]	4*h*	0.1197(1)	0.23643(5)	1/2	0.0153(4)
Ca(5)	4*g*	0.2780(1)	0.10283(6)	0	0.0125(3)
Mn(1)	4*g*	0.21570(1)	0.45583(5)	0	0.0131(2)
Mn(2)	4*g*	0.3790(1)	0.25860(6)	0	0.0137(3)
Mn(3)	4*g*	0.4686(5)	0.2284(3)	0	0.0137(3)
Sb(1)	2*c*	0	1/2	0	0.0115(1)
Sb(2)	4*h*	0.19436(4)	0.00213(2)	1/2	0.0131(1)
Sb(3)	4*h*	0.37104(4)	0.19215(2)	1/2	0.0124(1)
Sb(4)	4*g*	0.03448(3)	0.14865(2)	0	0.0105(1)
Sb(5)	4*g*	0.18539(4)	0.33212(1)	0	0.0099(1)

[a]U_{eq} is defined as one-third of the trace of the orthogonalized U_{ij} tensor. [b]Mixed-occupied Ca/Ce site, refined freely as 95(1)% Ca and 5% Ce. [c]Mixed-occupied Ca/Ce site, refined freely as 80(1)% Ca and 20% Ce. [d]Mixed-occupied Ca/Ce site, refined freely as 93(1)% Ca and 7% Ce. [e]Mixed-occupied Ca/Ce site, refined freely as 87(1)% Ca and 13% Ce.

Table 3.8. Atomic Coordinates and Equivalent Isotropic Displacement Parameters (U_{eq}[a]) for $Ca_{8.15}Pr_{0.85}Mn_4Sb_9$

Atom	Wyckoff Site	*x*	*y*	*z*	U_{eq} (Å^2)
A(1)[b]	2*a*	0	0	0	0.0127(9)
A(2)[c]	4*h*	0.3613(1)	0.36135(6)	1/2	0.0190(5)
A(3)[d]	4*h*	0.0538(1)	0.40781(7)	1/2	0.0148(6)
A(4)[e]	4*h*	0.1193(1)	0.23657(6)	1/2	0.0153(5)
Ca(5)	4*g*	0.2779(1)	0.10285(8)	0	0.0135(4)
Mn(1)	4*g*	0.2158(1)	0.45583(6)	0	0.0138(3)
Mn(2)	4*g*	0.3790(1)	0.25857(7)	0	0.0137(4)
Mn(3)	4*g*	0.4676(9)	0.2283(5)	0	0.0137(4)
Sb(1)	2*c*	0	1/2	0	0.0119(2)
Sb(2)	4*h*	0.19431(5)	0.00219(3)	1/2	0.0131(1)
Sb(3)	4*h*	0.37098(5)	0.19214(3)	1/2	0.0126(1)
Sb(4)	4*g*	0.03440(5)	0.14863(3)	0	0.0108(1)
Sb(5)	4*g*	0.18579(5)	0.33212(3)	0	0.0102(1)

[a]U_{eq} is defined as one-third of the trace of the orthogonalized U_{ij} tensor. [b]Mixed-occupied Ca/Pr site, refined freely as 98(1)% Ca and 2% Pr. [c]Mixed-occupied Ca/Pr site, refined freely as 79(1)% Ca and 21% Pr. [d]Mixed-occupied Ca/Pr site, refined freely as 93(1)% Ca and 7% Pr. [e]Mixed-occupied Ca/Pr site, refined freely as 86(1)% Ca and 14% Pr.

Table 3.9. Atomic Coordinates and Equivalent Isotropic Displacement Parameters (U_{eq}[a]) for $Ca_{8.11}Nd_{0.89}Mn_4Sb_9$

Atom	Wyckoff Site	*x*	*y*	*z*	U_{eq} (Å^2)
A(1)[b]	2*a*	0	0	0	0.0125(8)
A(2)[c]	4*h*	0.3614(1)	0.36195(5)	1/2	0.0167(4)
A(3)[d]	4*h*	0.0541(1)	0.40801(6)	1/2	0.0145(5)
A(4)[e]	4*h*	0.1190(1)	0.23665(5)	1/2	0.0132(4)
Ca(5)	4*g*	0.2777(1)	0.10302(7)	0	0.0128(3)
Mn(1)	4*g*	0.2159(1)	0.45594(5)	0	0.0132(3)
Mn(2)	4*g*	0.3789(1)	0.25854(6)	0	0.0137(3)
Mn(3)	4*g*	0.4678(9)	0.2289(5)	0	0.0137(3)
Sb(1)	2*c*	0	1/2	0	0.0113(1)
Sb(2)	4*h*	0.19429(4)	0.00226(2)	1/2	0.0125(1)
Sb(3)	4*h*	0.37089(4)	0.19218(2)	1/2	0.0122(1)
Sb(4)	4*g*	0.03420(4)	0.14862(2)	0	0.0101(1)
Sb(5)	4*g*	0.18592(4)	0.33216(2)	0	0.0095(1)

[a]U_{eq} is defined as one-third of the trace of the orthogonalized U_{ij} tensor. [b]Mixed-occupied Ca/Nd site, refined freely as 99(1)% Ca and 1% Nd. [c]Mixed-occupied Ca/Nd site, refined freely as 77(1)% Ca and 23% Nd. [d]Mixed-occupied Ca/Nd site, refined freely as 92(1)% Ca and 8% Nd. [e]Mixed-occupied Ca/Nd site, refined freely as 87(1)% Ca and 3% Nd.

Table 3.10. Atomic Coordinates and Equivalent Isotropic Displacement Parameters (U_{eq}[a]) for $Ca_{7.88}Sm_{1.12}Mn_4Sb_9$

Atom	Wyckoff Site	*x*	*y*	*z*	U_{eq} (Å^2)
A(1)[b]	2*a*	0	0	0	0.0119(7)
A(2)[c]	4*h*	0.36236(7)	0.36183(4)	1/2	0.0159(3)
A(3)[d]	4*h*	0.05733(10)	0.40843(5)	1/2	0.0170(4)
A(4)[e]	4*h*	0.12025(9)	0.23646(5)	1/2	0.0141(4)
Ca(5)	4*g*	0.27873(12)	0.10212(7)	0	0.0123(3)
Mn(1)	4*g*	0.21695(10)	0.45552(5)	0	0.0148(3)
Mn(2)	4*g*	0.38041(10)	0.25809(6)	0	0.0134(3)
Mn(3)	4*g*	0.4666(8)	0.2292(5)	0	0.0134(3)
Sb(1)	2*c*	0	1/2	0	0.0117(1)
Sb(2)	4*h*	0.19379(4)	0.00173(2)	1/2	0.0123(1)
Sb(3)	4*h*	0.37229(4)	0.19172(2)	1/2	0.0123(1)
Sb(4)	4*g*	0.03498(4)	0.14862(2)	0	0.0102(1)
Sb(5)	4*g*	0.18701(4)	0.33164(2)	0	0.0096(1)

[a]U_{eq} is defined as one-third of the trace of the orthogonalized U_{ij} tensor. [b]Mixed-occupied Ca/Sm site, refined freely as 98(1)% Ca and 2% Sm. [c]Mixed-occupied Ca/Sm site, refined freely as 71(1)% Ca and 29% Sm. [d]Mixed-occupied Ca/Sm site, refined freely as 88(1)% Ca and 12% Sm. [e]Mixed-occupied Ca/Sm site, refined freely as 84(1)% Ca and 16% Sm.

Table 3.11. Important Interatomic Distances (Å) and Angles (degree) for $Ca_{8.27}La_{0.73}Mn_4Sb_9$ and $Ca_{7.88}Sm_{1.12}Mn_4Sb_9$

$Ca_{8.27}La_{0.73}Mn_4Sb_9$		**$Ca_{7.88}Sm_{1.12}Mn_4Sb_9$**	
Mn1–Sb1	2.850(1)	Mn1–Sb1	2.861(1)
Mn1–Sb2	2.766(7) × 2	Mn1–Sb2	2.7505 (7) × 2
Mn1–Sb5	2.756(1)	Mn1–Sb5	2.752(1)
Mn2–Sb3	2.742(1) × 2	Mn2–Sb3	2.7301(7) × 2
Mn2–Sb4	2.822(1)	Mn2–Sb4	2.808(1)
Mn2–Sb5	2.905(1)	Mn2–Sb5	2.892(1)
Mn3–Sb3	2.730(3) × 2	Mn3–Sb3	2.712(5) × 2
Mn3–Sb4	2.844(7)	Mn3–Sb4	2.82 (1)
Mn3–Sb5	3.009(7)	Mn3–Sb5	3.04 (1)
Sb1–Mn1–Sb2	114.88(3)× 2	Sb1–Mn1–Sb2	104.54(3) ×2
Sb1–Mn1–Sb5	102.11(4)	Sb1–Mn1–Sb5	102.27(4)
Sb2–Mn1–Sb2	113.30(5)	Sb2–Mn1–Sb2	113.77(4)
Sb2–Mn1–Sb5	114.92(3) × 2	Sb2–Mn1–Sb5	114.88(3) ×2
Sb3–Mn2–Sb3	114.87(6)	Sb3–Mn2–Sb3	115.10(5)
Sb3–Mn2–Sb4	114.37(3)× 2	Sb3–Mn2–Sb4	114.62(3) ×2
Sb3–Mn2–Sb5	105.81(4)× 2	Sb3–Mn2–Sb5	105.61(3) ×2
Sb4–Mn2–Sb5	99.55(5)	Sb4–Mn2–Sb5	98.94(4)
Sb3–Mn3–Sb3	115.7(2)	Sb3–Mn3–Sb3	116.3(4)
Sb3–Mn3–Sb4	114.0(1)×2	Sb3–Mn3–Sb4	114.8(2) ×2
Sb3–Mn3–Sb5	105.7(1)×2	Sb3–Mn3–Sb5	104.6(2) ×2
Sb4–Mn3–Sb5	99.6(2)	Sb4–Mn3–Sb5	98.6(3)
Mn1–Sb5–Mn2	116.13(4)	Mn1–Sb5–Mn2	116.31(4)
Mn1–Sb5–Mn3	124.2(1)	Mn1–Sb5–Mn3	123.9(1)
Mn2–Sb5–Mn3	119.6(1)	Mn2–Sb5–Mn3	119.8(1)

Table 3.12. Comparison between measured and expected effective moments in $Ca_{9-x}RE_xMn_4Sb_9$ series (*RE*= La, Ce, Pr, Nd and Sm).

	$Ca_{8.27}La_{0.73}Mn_4Sb_9$	**$Ca_{8.16}Ce_{0.84}Mn_4Sb_9$**	**$Ca_{8.15}Pr_{0.85}Mn_4Sb_9$**	**$Ca_{8.11}Nd_{0.89}Mn_4Sb_9$**	**$Ca_{7.88}Sm_{1.12}Mn_4Sb_9$**
Measured $\mu_{eff}(\mu_B)$	4.89	10.63	10.95	12.29	11.87
Expected $\mu_{eff}(\mu_B)$	5.92	12.06	12.19	12.32	11.88

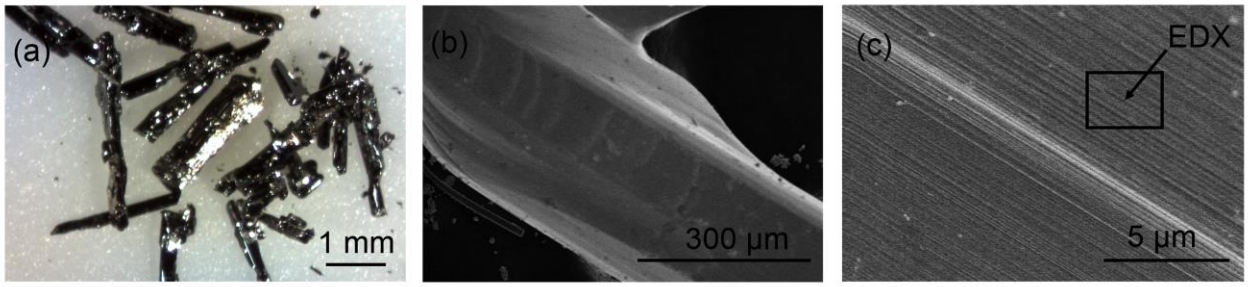

Figure 3.1. (a) optical microscope of $Ca_{8.11}Nd_{0.89}Mn_4Sb_9$; (b) and (c) represented scanning electron microscope (SEM) images, and squared part was energy dispersive X-ray analysis (EDS) area.

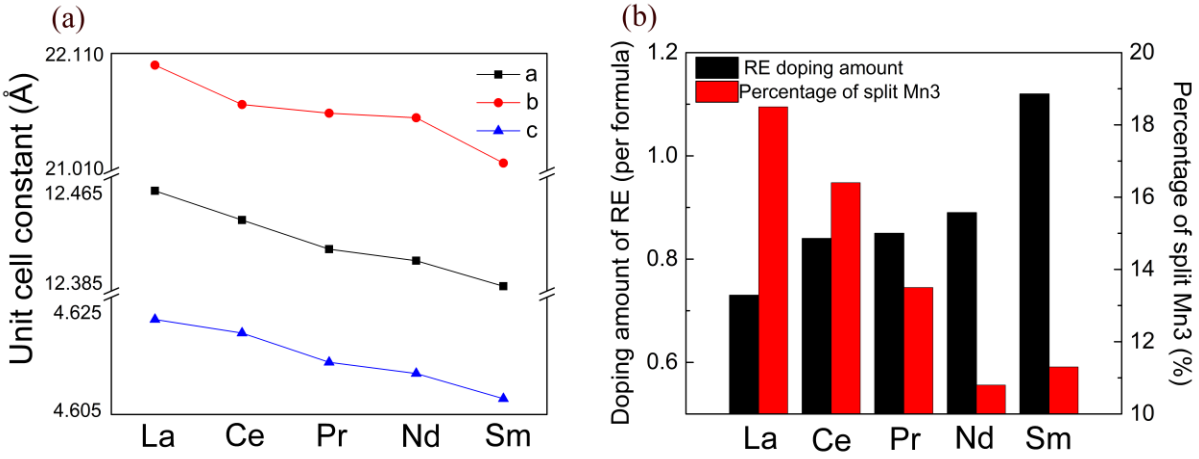

Figure 3.2. Trends of unit cell constants showed in (a); (b) represented trend of *RE* doping amount (in black) and percentage of split Mn3 (in red) in $Ca_{9-x}RE_xMn_4Sb_9$ series (*RE*= La, Ce, Pr, Nd and Sm).

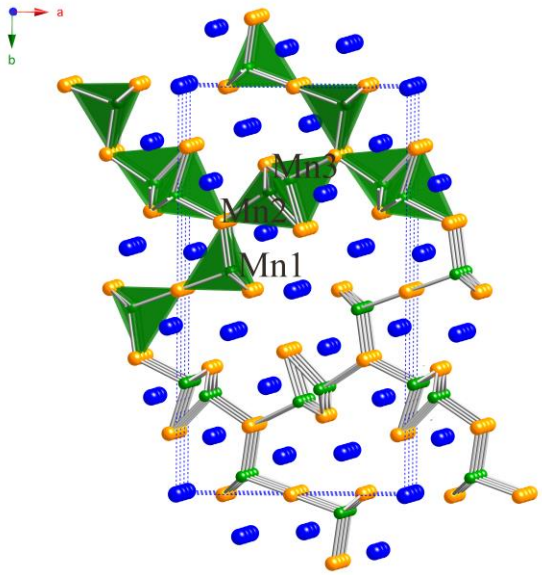

Figure 3.3. Unit cell of $Ca_{9-x}RE_xMn_4Sb_9$ (*RE*= La, Ce, Pr, Nd and Sm). Cations for Ca and *RE* atoms are drawn in blue spheres, which are co-occupied in some sites. Mn atoms are drawn in green spheres. Sb atoms are drawn in orange spheres. Three Mn positions are labeled.

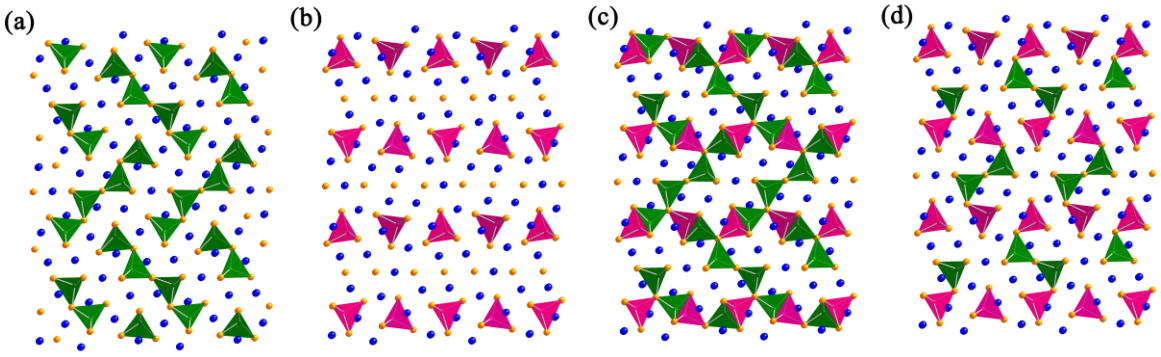

Figure 3.4. Schematic representation of the structural relationship between $Ca_9Mn_4Bi_9$ and $Ca_{9-x}RE_xMn_4Sb_9$ (*RE*= La, Ce, Pr, Nd and Sm).

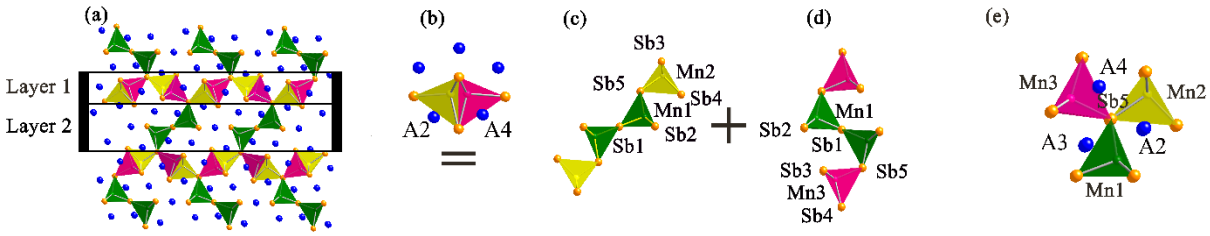

Figure 3.5. Schematic representation of split Mn3 exists and explanation of tendency of Mn3 split percentage in $Ca_{9-x}RE_xMn_4Sb_9$ series (*RE*= La, Ce, Pr, Nd and Sm).

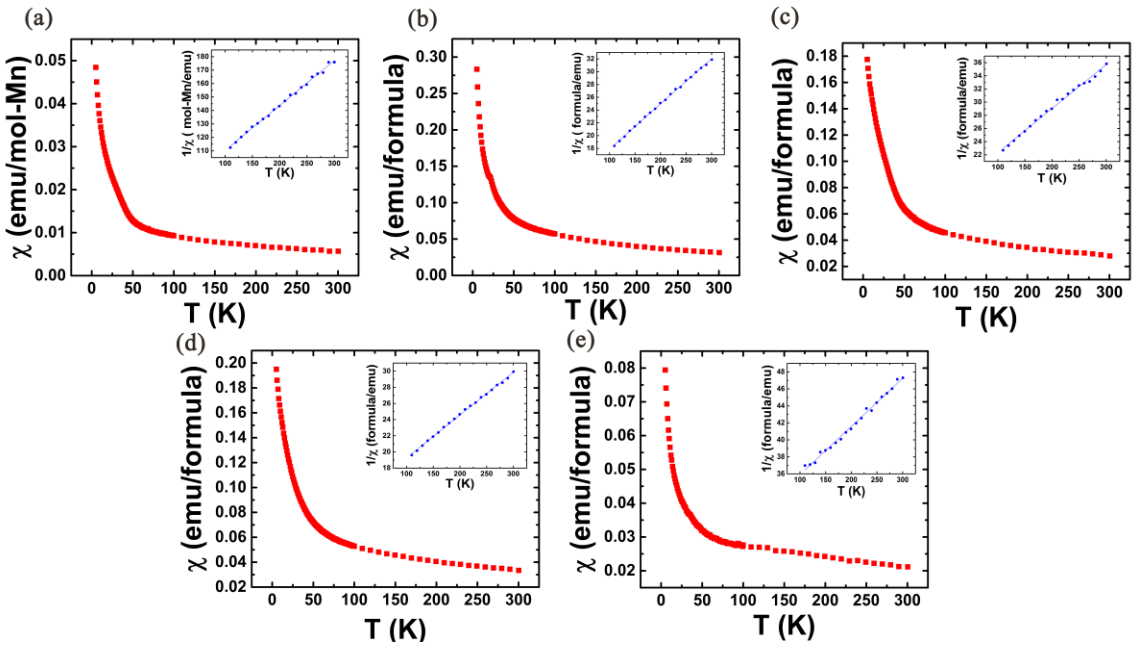

Figure 3.6. Temperature dependent magnetic susceptibility for polycrystalline $Ca_{9-x}RE_xMn_4Sb_9$: (a): La, (b): Ce, (c): Pr, (d): Nd and (e): Sm. The inset shows the temperature dependence of the inverse magnetic susceptibility. The solid line is the linear-fit of the data, according to the Curie–Weiss law.

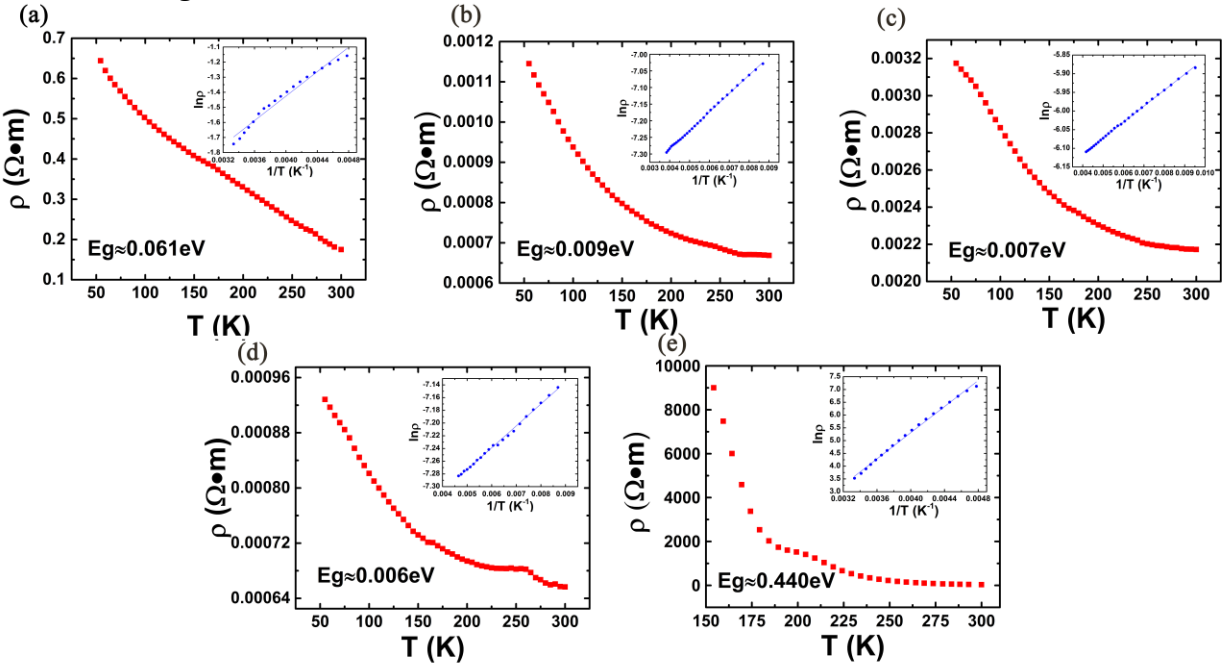

Figure 3.7. Temperature dependent electrical resistivity for single crystal $Ca_{9-x}RE_xMn_4Sb_9$: (a): La, (b): Ce, (c): Pr, (d): Nd and (e): Sm ρ(T) and lnρ(1/T) (inset) are shown.

REFERENCES

1. (a) Kauzlarich, S. M. Ed. Chemistry, Structure and Bonding in Zintl Phases and Ions; VCH: New York, **1996** and the references therein. (b) Corbett, J. D. *Angew. Chem., Int. Ed.* **2000**, *39*, 670.

2. Lee, C. S.; Miller, G. J. *J. Am. Chem. Soc.* **2000**, *122*, 4937.

3. Mozharivskyj, Y.; Choe, W.; Pecharsky, A. O.; Miller, G. J. *J. Am. Chem. Soc.* **2003**, *125*, 15183.

4. Chen, L.; Corbett, J. D. *J. Am. Chem. Soc.* **2003**, *125*, 1170.

5. Houben, A.; Müller, P.; von Appen, J.; Lueken, H.; Niewa, R.; Dronskowski, R. *Angew. Chem., Int. Ed.* **2005**, *44*, 7212.

6. Poudeu, P. F. P.; D'Angelo, J.; Kong, H. J.; Downey, A.; Short, J. L.; Pcionek, R.; Hogan, T. P.; Uher, C.; Kanatzidis, M. G. *J. Am. Chem. Soc.* **2006**, *128*, 14347.

7. Lupu, C.; Downie, C.; Guloy, A. M.; Albright, T. A.; Mao, J.-G. *J. Am. Chem. Soc.* **2004**, *126*, 4386.

8. Brown, S. R.; Kauzlarich, S. M.; Gascoin, F.; Snyder, G. J. *Chem. Mater.* **2006**, *18*, 1873.

9. Brown, S. R.; Toberer, E. S.; Ikeda, T.; Cox, C. A.; Gascoin, F.; Kauzlarich, S. M.; Snyder, G. J. *Chem. Mater*. **2008**, *20*, 3412.

10. Kimber, S. A.; Kreyssig, A.; Zhang, Y.; Jeschke, H. O.; Valenti, R.; Yokaichiya, F.; Colombier, E.; Yan, J.; Hansen, T. C.; Chatterji, T.; McQueeney, R. J.; Canfield, P. C.; Goldman, A. I.; Argyriou, D. N. *Nat. Mater*. **2009**, *8*, 471.

11. Goforth, A. M.; Hope, H.; Condron, C. L.; Kauzlarich, S. M.; Jensen, N.; Klavins, P.; MaQuilon, S.; Fisk, Z. *Chem. Mater*. **2009**, *21*, 4480.

12. Schäfer, H.; Eisenmann, B.; Müller, W. *Angew. Chem., Int. Ed*. **1973**, *12*, 694.

13. Schäfer, H. *Annu. Rev. Mater. Sci.* **1985**, *15*, 1.

14. Nesper, R. *Prog. Solid. St. Chem*. **1990**, 20, 1.

15. Nesper, R. *Angew. Chem., Int. Ed*. **1991**, *30*, 789.

16. Cahen, D. *Chem. Mater.* **1998**, *10*, 2596.

17. Nistor, R. A.; Newns, D. M.; Martyna, G. J. *ACS Nano*. **2011**, *5*, 3096.

18. Suh, J.; Park, T. E.; Lin, D. Y.; Fu, D. Y.; Wu, J. Q. *Nano Lett.* **2014**, *14*, 6976.

19. Aydemir, U.; Zevalkink, A.; Ormeci, A.; Gibbs, Z. M.; Bux, S.; Snyder, G. J. *Chem. Mater*. **2015**, *27*, 1622.

20. Valentin, C. D.; Pacchioni, G.; Selloni, A. *Chem. Mater.* **2005**, *17*, 6656.

21. Zhang, H. Y.; Pokhrel, S.; Ji, Z. X.; Meng, H.; Wang, X.; Lin, S. J.; Liu, R.; Xia, T.; Mädler, L.; Nel, A. E. *J. Am. Chem. Soc*. **2014**, *136*, 6406.

22. Jorge, M. E. M.; Nunes, M. R.; Maria, R. S.; Sousa, D. *Chem. Mater.* **2005**, *17*, 2069.

23. Carvalho, M. D.; Borges, R. P.; Godinho, M. *Chem. Mater.* **2005**, *17*, 4852.

24. Yu, B.; Zebarjadi, M.; Wang, H.; Lukas, K.; Wang, H. Z.; Wang, D. Z.; Ren, Z. F. *Nano Lett.* **2012**, *12*, 2077.

25. Brechtel, E.; Cordier, G.; Schäfer, H. *Z. Naturforsch. B.* **1979**, *34*, 1229.

26. Bobev, S.; Thompson, J. D.; Sarrao, J. L.; Olmstead, M. M.; Hope, H.; Kauzlarich, S. M. *Inorg. Chem*. **2004**, *43*, 5044.

27. Xia, S. Q.; Bobev, S. *J. Am. Chem. Soc*. **2007**, *129*, 10011.

28. Xia, S. Q.; Bobev, S. *Chem. Mater*. **2010**, *22*, 840.

29. Liu, X. C.; Wu, Z.; Xia, S. Q.; Tao, X. T.; Bobev, S. *Inorg. Chem.* **2015**, *54*, 947.

30. *SMART* and *SAINT*; Bruker AXS Inc.: Madison, WI, **2002**.

31. Sheldrick, G. M. SADABS. University of Go¨ttingen, Germany, **2003**.

32. Sheldrick, G. M. SHELXTL. University of Go¨ttingen, Germany, **2001**.

33. Gelato, L. M.; Parthe, E. *J. Appl. Crystallogr*. **1987**, *20*, 139.

34. Pauling, L. The Nature of the Chemical Bond, Cornell University Press, Ithaca NY, **1960**.

35. Cordier, G.; Schaefer, H. *Z. Naturforsch. B.* **1976**, *31*, 1459.

36. Rehr, A.; Kuromoto, T. Y.; Kauzlarich, S. M.; Webb, D. J. *Chem. Mater*. **1994**, *6*, 93.

37. Kim, H.; Condron, C. L.; Holm, A. P.; Kauzlarich, S. M. *J. Am. Chem. Soc.* **2000**, *122*, 10720.

38. Xia, S. Q; Bobev, S. *Inorg. Chem*. **2008**, *47*, 1919.

39. Wang, Y; Stoyko, S.; Bobev, S. *Inorg. Chem.* **2015**, *54*, 1931.

40. Kittel, C. Introduction to Solid State Physics, Seventh ed, Wiley, Hoboken, NJ, **1996**.

41. Sologub, O.; Vybornov, M.; Rogl, P.; and Hiebl, K. *J. Solid. State. Chem.* **1996**, *122*, 266.

42. Young, C. G. *Chem. Rev.* **1989**, *96*, 89.

43. Strobel, P.; Capponi, J. J.; Chaillout, C.; Marezio, M.; Tholence, J. L. *Nature.* **1987**, *327*, 306.

44. Kim, S. J.; Salvador, J.; Bilc, D.; Mahanti, S. D.; Kanatzidis, M. G. *J. Am. Chem. Soc.* **2001**, *123*, 12704.

Chapter 4

CONCLUSIONS

4.1 Brief Summary of This Work

In this thesis, we report eight new compounds in two chapters: (1) quaternary pnictides with complex, noncentrosymmetric structures: Synthesis and Structural Characterization of the New Zintl Phases $Na_{11}Ca_2Al_3Sb_8$, $Na_4CaGaSb_3$, and $Na_{15}Ca_3In_5Sb_{12}$ [1]. Three new Zintl phases were produced: $Na_{11}Ca_2Al_3Sb_8$, $Na_4CaGaSb_3$, and $Na_{15}Ca_3In_5Sb_{12}$ in this chapter. Three different structure types were shown for each compound and the structure relationship with $Na_3In_2Bi_3$ [2] was also discussed. By discovery of two different types of Na cations, interlayer and intralayer, it provides new examples to prove the importance of cations as structure direction factor in Zintl phases. (2) Efficient Tailoring of Band Gap Induced by Rare Earth (*RE*) Metals Doping: Determining Structure and Properties of Narrow-Gap Semiconductor $Ca_{9-x}RE_xMn_4Sb_9$ (*RE* = La, Ce, Pr, Nd and Sm). A new structure phase of $Ca_{9-x}RE_xMn_4Sb_9$ (*RE* = La, Ce, Pr, Nd and Sm) were synthesized. By replacing Ca by *RE* atoms, the new series achieve charge balanced and represent narrow gap semiconductor properties.

4.2 Future Prospects

Based on the successfully doping for "9-4-9" system, in future we may still work on RE doping exploration with known ternary systems we investigate before, such as "21-4-18" [3]. The difficulty may be how to control the amount of rare earth in different system and the temperature profile of reaction due to high melting point of rare earth elements.

REFERENCES

1. Wang, Y.; Stoyko, S.; Bobev, S. *Inorg. Chem*. **2015**, *54*, 1931.

2. Bobev, S.; Sevov, S. C. *J. Solid State Chem*. **2001**, *163*, 436.

3. Xia, S. Q.; Bobev, S. *Inorg. Chem*. **2008**, *47*, 1919.

Appendix A

A HANDY LIST OF EIGHT NEW COMPOUNDS AND THEIR SPACE GROUP INFORMATION

1. $Na_{11}Ca_2Al_3Sb_8$ *Pmn2₁*
2. $Na_4CaGaSb_3$ *Pc*
3. $Na_{15}Ca_3In_5Sb_{12}$ *Pmc2₁*
4. $Ca_{8.27}La_{0.73}Mn_4Sb_9$ *Pbam*
5. $Ca_{8.16}Ce_{0.84}Mn_4Sb_9$ *Pbam*
6. $Ca_{8.15}Pr_{0.85}Mn_4Sb_9$ *Pbam*
7. $Ca_{8.11}Nd_{0.89}Mn_4Sb_9$ *Pbam*
8. $Ca_{7.88}Sm_{1.12}Mn_4Sb_9$ *Pbam*

Appendix B

REPRINT PERMISSION LETTERS

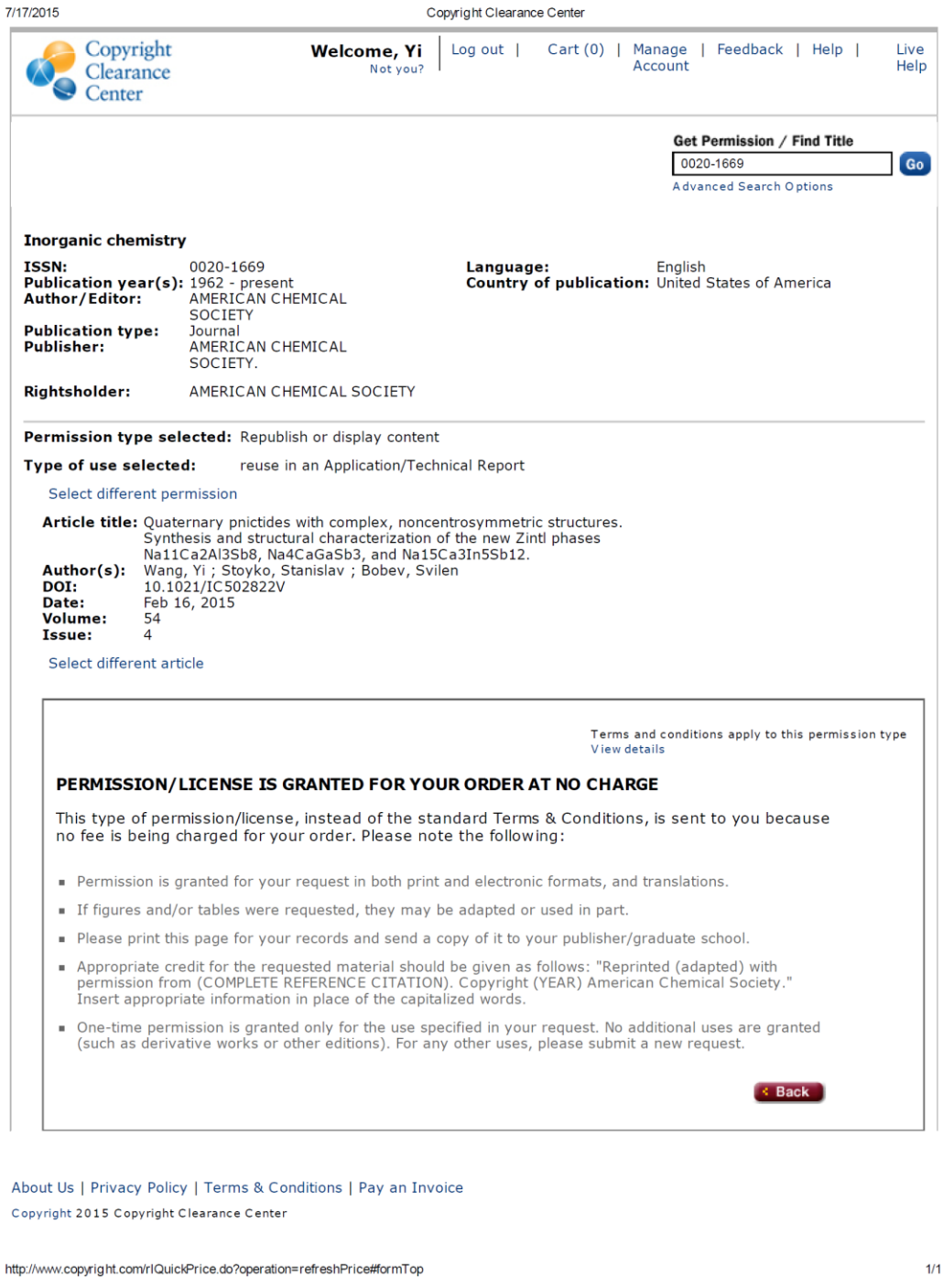

7/17/2015 Copyright Clearance Center

Copyright Clearance Center

Welcome, Yi
Not you?

Log out | Cart (0) | Manage Account | Feedback | Help | Live Help

Get Permission / Find Title
0020-1669 Go
Advanced Search Options

Inorganic chemistry

ISSN: 0020-1669
Publication year(s): 1962 - present
Author/Editor: AMERICAN CHEMICAL SOCIETY
Publication type: Journal
Publisher: AMERICAN CHEMICAL SOCIETY.
Language: English
Country of publication: United States of America

Rightsholder: AMERICAN CHEMICAL SOCIETY

Permission type selected: Republish or display content

Type of use selected: reuse in an Application/Technical Report

Select different permission

Article title: Quaternary pnictides with complex, noncentrosymmetric structures. Synthesis and structural characterization of the new Zintl phases $Na_{11}Ca_2Al_3Sb_8$, $Na_4CaGaSb_3$, and $Na_{15}Ca_3In_5Sb_{12}$.
Author(s): Wang, Yi ; Stoyko, Stanislav ; Bobev, Svilen
DOI: 10.1021/IC502822V
Date: Feb 16, 2015
Volume: 54
Issue: 4

Select different article

Terms and conditions apply to this permission type
View details

PERMISSION/LICENSE IS GRANTED FOR YOUR ORDER AT NO CHARGE

This type of permission/license, instead of the standard Terms & Conditions, is sent to you because no fee is being charged for your order. Please note the following:

- Permission is granted for your request in both print and electronic formats, and translations.
- If figures and/or tables were requested, they may be adapted or used in part.
- Please print this page for your records and send a copy of it to your publisher/graduate school.
- Appropriate credit for the requested material should be given as follows: "Reprinted (adapted) with permission from (COMPLETE REFERENCE CITATION). Copyright (YEAR) American Chemical Society." Insert appropriate information in place of the capitalized words.
- One-time permission is granted only for the use specified in your request. No additional uses are granted (such as derivative works or other editions). For any other uses, please submit a new request.

Back

About Us | Privacy Policy | Terms & Conditions | Pay an Invoice

Copyright 2015 Copyright Clearance Center

http://www.copyright.com/rlQuickPrice.do?operation=refreshPrice#formTop 1/1